Compensation of Incoherent Errors in the Precise Implementation of Effective Hamiltonians for Quantum Information Processing

by

Amro M. Farid

S.B. Mechanical Engineering
Massachusetts Institute of Technology 2000

Submitted to the Mechanical Engineering
in partial fulfillment of the requirements for the degree of

Master of Science in Mechanical Engineering

at the

MASSACHUSETTS INSTITUTE OF TECHNOLOGY

June 2002

Author . . . .
Mechanical Engineering
October 17, 2012

Certified by . . . .
Seth Lloyd
Professor of Mechanical Engineering
Thesis Supervisor

Certified by . . . .
David Cory
Professor of Nuclear Engineering
Thesis Supervisor

Accepted by . . . .
Ain Sonin
Chairman, Department Committee on Graduate Students

Compensation of Incoherent Errors in the Precise Implementation of Effective Hamiltonians for Quantum Information Processing

by

Amro M. Farid

Submitted to the Mechanical Engineering
on October 17, 2012, in partial fulfillment of the
requirements for the degree of
Master of Science in Mechanical Engineering

Abstract

This thesis sets out to present an algorithm for compensation of incoherent errors in quantum information processing (QIP). In particular, it addresses the incoherent errors that arise from RF inhomogeneity in a liquid state NMR system. It briefly describes NMR's place in QIP experimental developments and explains the need to eliminate the errors introduced by RF inhomogeneity. An algorithm for compensation is proposed provided that one has prior knowledge of the system Hamiltonian and a measurement of the degree of RF inhomogeneity. The algorithm was used to create two sets of RF pulses; an uncompensated set that did not use the RF inhomogeneity measurement and a more robust set that did use the measurement. Simulation results indicate that all of the new pulses reduced the error by approximately an order of magnitude for the measured RF inhomgeneity, as well as for most other types of RF inhomogeneity. This result was verified in experiment, where correlations were improved by 0.024 on average. In total, errors due to RF inhomogeneity were reduced by a factor of six.

Thesis Supervisor: Seth Lloyd
Title: Professor of Mechanical Engineering

Thesis Supervisor: David Cory
Title: Professor of Nuclear Engineering

Acknowledgments

I would like to thank Professors David Cory and Seth Lloyd for exposing me to the new and exciting field of Quantum Information Processing. Their combined knowledge of the field has gone a long way to further my understanding and illuminate particularly difficult concepts. This project has also broadened my understanding of control theory, signals and systems, quantum mechanics, and electromagnetism. It has been a tremendous opportunity to work within Professor Cory's laboratory which has provided the spectrometers and the computers required for this research. Lastly, I would like to thanks Professors Cory and Lloyd for academically and professionally advising me over the last two years.

I would also like to thank Marco Pravia for our combined efforts on this project. He has made great efforts within the same field which have helped me greatly in the completion of this thesis. I would like to thank especially Evan Fortunato, Greg Boutis, Grum Teklemariam, and Yaakov Weinstein for many stimulating conversations over the last two years. Especially during my first year, they have often taken the time to impart their knowledge to me as well as other less senior members of the research group. I also would like to thank the other members of the group for providing a very helpful and cooperative work environment.

Many people in my personal life have helped me in producing this document. First, I must thank Paula Deardon. With respect to my MIT life, she has provided unquestionable moral support and encouragement, even during the most trying times of the last two years. I also thank Jan Meyer for encouragement over the last year and a half. Finally, I thank my family. Even from New York, my twin sister, Nora has an amazing sense to know when I most need support. Sarah's comical anecdotes of middle school life lighten even the most stressful days. My mother, Yomn Elsayed is just always there. Lastly, I thank my father Mohsen Farid for sparking my interest in physics at a very young age and encouraging me to continue with it for graduate study.

This thesis sets out to present an algorithm for compensation of incoherent errors in quantum information processing (QIP). In particular, it addresses the incoherent errors that arise from RF inhomogeneity in a liquid state NMR system. It briefly describes NMR's place in QIP experimental developments and explains the need to eliminate the errors introduced by RF inhomogeneity. An algorithm for compensation is proposed provided that one has prior knowledge of the system Hamiltonian and a measurement of the degree of RF inhomogeneity. The algorithm was used to create two sets of RF pulses; an uncompensated set that did not use the RF inhomogeneity measurement and a more robust set that did use the measurement. Simulation results indicate that all of the new pulses reduced the error by approximately an order of magnitude for the measured RF inhomgeneity, as well as for most other types of RF inhomogeneity. This result was verified in experiment, where correlations were improved by 0.024 on average. In total, errors due to RF inhomogeneity were reduced by a factor of six.

Acknowledgments

acknowledgements here

Contents

List of Figures

Chapter 1

Introduction

1.1 Background on QIP

Feynman, in 1982, proposed the idea of using dynamical systems governed by quantum mechanics to simulate quantum physics [1]. Quantum mechanical simulation is difficult on a classical computer. An N particle system's state requires a vector of 2^N elements, so for large N, just writing the wave function, let alone simulating its dynamics, is infeasible. A quantum information processor can act as an analog simulation of other quantum mechanical systems resources [4]. It can do this by mapping the simulated system's state to that of the quantum information processor and using a set of universal gates to enact the simulated dynamics. Additionally, Feynman's idea has been expanded to the use of quantum mechanical systems to do computations. This new field of Quantum Information Processing (QIP) has led to quantum mechanical search and factoring algorithms that give exponential speed improvements over their classical counterparts [2], [3]. (These algorithms would revolutionize the current field of encryption.)

The advantages of QIP arise from the ability of a quantum mechanical particle to be in a superposition of states. In classical computation, a bit is either $|0\rangle$ or $|1\rangle$; on or off. A qubit $|\psi\rangle$ can be in an arbitrary superposition of these two classical states; $|\psi\rangle = c_+|0\rangle + c_-|1\rangle$. Given some algorithm or function f, two classical computations are required to find the result f(0) and f(1), while only one quantum computation is required to do the same. This difference is magnified for an N qubit computation which can perform 2^N classical computations.

1.2 NMR as a paradigm for QIP

Recently, advances in QIP have included experiments. Quantum control has been demonstrated in quantum optics [5], [6] and nuclear magnetic resonance (NMR) [7], [8], [9]. Warren provides a summary of their advances [10]. NMR has been used to experimentally demonstrate quantum error correction [11], [12], quantum simulation [13], and quantum algorithms [14], [15] such as the quantum Fourier transform [16].

The NMR paradigm for QIP currently uses a solution of molecules dissolved in a liquid solvent. Usually the molecule will contain atomic nuclei that are spin 1/2 particles such as H^1 and C^{13}. Each of these spin 1/2 particles provide one qubit in the QIP. Although there are approximately Avagadro's number of molecules in the solution, the system does not have that many qubits. This is because solution dynamics remove the intermolecular dipolar coupling. (This leaves each of the molecules to be indifferentiable from the other.) As a result, the quantum information processing is carried out on an ensemble of molecules whose spin dynamics closely parallel the spin dynamics of an individual molecule. At room temperature, the state of the ensemble is highly mixed. The small imbalance between the spin up and spin down populations is on the order of 10^{-6} and provides the NMR signal [17].

1.3 Experimental Apparatus

The NMR spectrometer is composed of a static magnetic field, a probe, radio frequency transmitter. The probe includes an inductor coil that applies time varying magnetic fields to the sample. The direction of the static magnetic field is conventionally taken to be in the z direction. For QIP, its strength is usually on the order of 10 Tesla. Figure 1-1 shows a 9.6MHz magnet. Much like classical tops in the earth's gravitational field, this static magnetic field aligns nuclei with spin upwards or downwards. An alternating current, usually in the radio frequency range, is run through the inductor coil, and a time varying magnetic field of the same frequency is applied to the sample within. The addition of this secondary field allows for control of the spin system's orientation state.

The RF coil is also responsible for signal detection. Figure 1-2 shows a schematic diagram of the RF coil's dual function. In its first function, the gate is closed. A RF frequency current is amplified and then delivered to the sample as a magnetic field. In its

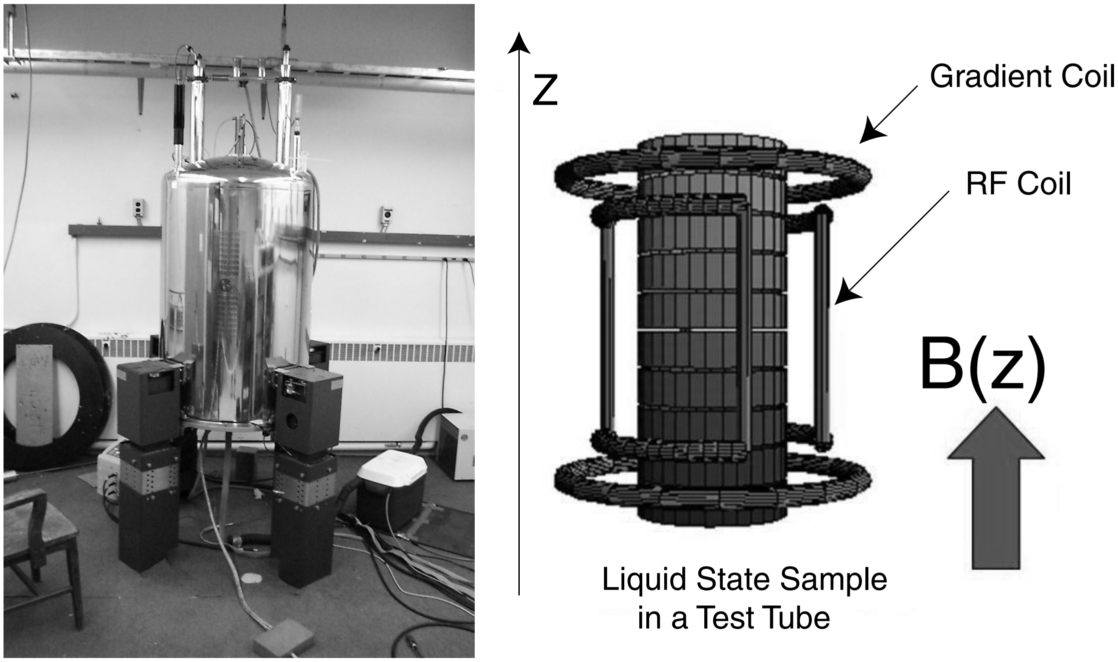

Figure 1-1: On the left is a photo of a 9.6T magnet. On the right, is a diagram of the RF coil that applies time varying magnetic fields to the sample within.

second state, when the spin system is not being excited, the gate is open. The spin system evolves freely, causes a time varying magnetic field which is detected as an alternating current in the coil. Because the current's frequency is on the order 400 megaHertz, it is convenient to mix the signal down to an audio signal.

1.4 Motivation for Robust Control

NMR provides a test-bed for investigating QIP experiments. Pulses can be applied experimentally to manipulate a spin system such that its final state is equivalent to the output of a chosen theoretical algorithm. One challenge in QIP is that the errors in the implementation of these pulses often cause a loss of information during the course of the algorithm. One type of error, called incoherent errors, occurs when the different parts of an ensemble have experimentally different evolutions. In NMR, this type of error is exemplified by inhomogeneity in the RF coil. Usually, the magnetic field strength within the RF coil is modelled as a spatially uniform. In actuality, due to fringe effects and imperfections in the coil, the

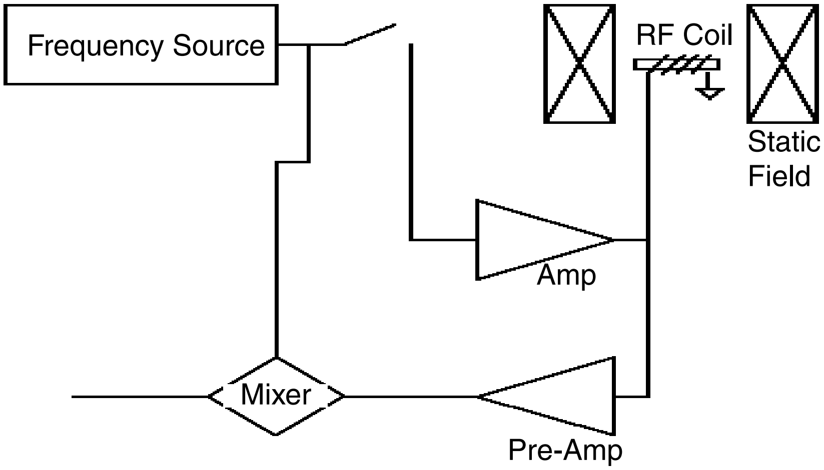

Figure 1-2: A schematic diagram of the RF coil's dual function; external control of the spin system and signal detection [18].

magnetic field strength varies spatially. The signal from the ensemble is a collection of evolutions based upon a distribution of the RF coil's magnetic field strengths.

Because these errors cause an exponential loss of information, it is critical that they be reduced. The proposed method is to develop a set of pulses that are insensitive towards variations in the pulse power. If a particular evolution does not require a high accuracy in the RF pulse power, then such evolution would be more capable of retaining information in the presence of RF inhomogeneities.

1.5 Overview of Approach

The approach to finding a set of robust control pulses that give desired evolutions is straightforward. Chapter 2 will acquaint the reader with detailed dynamics of a liquid state NMR system. Once the reader has gained knowledge of the system Hamiltonian, Chapter 3 will step back and define a metric for the experimental precision of an RF Pulse with respect to a desired theoretical evolution. It will continue by casting a direct relationship between RF inhomogeneity and this metric. Next, it will show a method of measuring the degree of RF inhomogeneity and use this information in the development of a compensation algorithm that yields robust control. Chapter 5 will discuss the experimental issues of realizing these robust pulses and then summarize their experimental performance relative to a non-robust method. Finally, Chapter 6 will discuss various aspects of this robust control method, explore its achievable limits and propose extensions of the method to other fields of control.

Chapter 2

Dynamics of Liquid State Nuclear Magnetic Resonance

The static magnetic field of the NMR apparatus aligns spin 1/2 particles into one of two eigenstates: the ground or up state and the excited or down state. This chapter will explain this physics, show how the spin states can be used as qubits and show how the spin system can be excited using time varying radio frequency magnetic field pulses.

2.1 Spin Wavefunctions, Operators, and Bra-Kets

A spin 1/2 particle is measured as having one of two discrete values of spin $\pm\hbar/2$ [19]. These two values can be mapped on to the standard basis vectors.

$$|0\rangle \doteq \begin{bmatrix} 1 \\ 0 \end{bmatrix} \qquad |1\rangle \doteq \begin{bmatrix} 0 \\ 1 \end{bmatrix} \tag{2.1}$$

where the ket notation of $|0\rangle$ and $|1\rangle$ refers to the positive and negative value of the z component of the spin respectively. A general spin state ψ is a superposition of these values[19],

$$|\psi\rangle = c_+|0\rangle + c_-|1\rangle = \begin{bmatrix} c_+ \\ c_- \end{bmatrix} \tag{2.2}$$

where $c_+^2 + c_-^2 = 1$. The dynamics of the spin state is given by the time independent Schrödinger's Equation,

$$\frac{d}{dt}|\psi(t)\rangle = \frac{-\imath}{\hbar}\mathcal{H}|\psi(t)\rangle \tag{2.3}$$

where $\mathcal{H}$ is the system Hamiltonian. For a time independent Hamiltonian, the evolution of the spin state is described by a unitary operation.

$$|\psi(\tau)\rangle = e^{-i\mathcal{H}\frac{\tau}{\hbar}}|\psi(0)\rangle \tag{2.4}$$

It is convenient to introduce the Pauli spin operators σ_x, σ_y and σ_z, and the identity operator as a basis of the Hamiltonian space.

$$\sigma_x = \begin{bmatrix} 0 & 1 \\ 1 & 0 \end{bmatrix} \quad \sigma_y = \begin{bmatrix} 0 & \imath \\ -\imath & 0 \end{bmatrix} \quad \sigma_z = \begin{bmatrix} 1 & 0 \\ 0 & -1 \end{bmatrix} \tag{2.5}$$

These operators are hermitian and have many useful mathematically and physically significant properties[19],

$$\sigma_i^2 = I_2, \quad \sigma_i^\dagger = \sigma_i, \quad \det(\sigma_i) = -1, \quad Tr(\sigma) = 0 \tag{2.6}$$

Additionally, they obey the anti-commutation relation $\{\sigma_i, \sigma_j\} = 2\delta_{ij}$, and the commutation relation $[\sigma_x, \sigma_y] = 2i\sigma_z$, which also holds for all cyclical permutations of the operators. Anti-cyclical permutations give a minus sign. These operators have the physical significance that they give the expectation value of the spin wave function $\langle\sigma\rangle$ with respect to the chosen cartesian axis[19].

$$\langle\sigma_x\rangle = \langle\psi|\sigma_x|\psi\rangle \quad \langle\sigma_y\rangle = \langle\psi|\sigma_y|\psi\rangle \quad \langle\sigma_z\rangle = \langle\psi|\sigma_z|\psi\rangle \tag{2.7}$$

$\langle x\rangle$ is the expectation value of an arbitrary operator x. The bra notation $\langle x|$ is the complex conjugate transpose of the ket notation $|x\rangle$, and hence the bra-ket defines $\langle x|x\rangle$ an inner product and the ket-bra $|x\rangle\langle x|$ defines an outer product. Additionally, it is important to notice that a spin with an expectation value of unity along a given axis will have a non-zero expectation value along other axes.

2.2 A Spin 1/2 Particle in the Static Magnetic Field

In a magnetic field $\vec{B}$, the energy of a spin is similar to that of a classical magnetic moment $\vec{\mu}$. It will align or anti-align with the field and have an energy of [20],

$$E = -\vec{\mu} \cdot \vec{B} \tag{2.8}$$

Similarly, a spin 1/2 particle's magnetic moment is given by[21],

$$\mu = \gamma \hbar m \tag{2.9}$$

where γ is the gyromagnetic ratio, and m is the value of the spin. For a static field $\vec{B} = B_0 \hat{z}$, the matrix representation of the Hamiltonian (often referred to as the Zeeman Hamiltonian) is[21],

$$\mathcal{H} = \frac{\gamma \hbar B_o}{2} \sigma_z \tag{2.10}$$

2.3 Thermal Excitation and the Density Matrix

A typical liquid state NMR sample, placed in a test tube, will have many spin 1/2 particles. Spins are thermally excited away from the ground state according to the Boltzmann distribution,

$$w_{\pm} = \frac{N_{\pm}}{N} = \frac{e^{\frac{\gamma \hbar B_o}{2K_b T}}}{\sum_{m=\frac{-1}{2}}^{\frac{1}{2}} e^{\frac{m\gamma \hbar B_o}{K_b T}}} \approx \frac{1}{2} \pm \frac{\gamma \hbar B_0}{4 K_b T} \tag{2.11}$$

so that a fraction w_+ are in the ground state and w_- are in the excited state[17]. This mixed ensemble can not be represented with a single wave function, and requires the introduction of the density matrix ρ[19],

$$\rho = \sum_i w_i |\psi_i >< \psi_i| \tag{2.12}$$

whose evolution is given by the Liouville-Von Neumann equation;

$$\frac{d}{dt}\rho(t) = \frac{-\imath}{\hbar}[\mathcal{H}, \rho(t)] \tag{2.13}$$

For a time independent Hamiltonian, the evolution of the density matrix is given by a unitary transformation.

$$\rho(\tau) = e^{-\imath\mathcal{H}\frac{\tau}{\hbar}}\rho(0)e^{\imath\mathcal{H}\frac{\tau}{\hbar}} \tag{2.14}$$

Additionally, the concept of an expectation value is replaced by the ensemble average[19],

$$[X] = \sum_i w_i < \psi_i|x|\psi_i >= Tr(\rho X) \tag{2.15}$$

2.4 The External Hamiltonian and the Rotating Frame

In addition to the B_0 static field, the NMR spectrometer uses an inductor coil to create small magnetic fields oriented along an axis orthogonal to $\hat{z}$. Momentarily assuming a static magnetic field B_1 oriented along $\hat{x}$, and setting $\hbar$ to unity (for the remainder of this thesis), the Hamiltonian would be,

$$\mathcal{H} = \frac{-\gamma B_0}{2}\left(\sigma_z + \frac{B_1}{B_0}\sigma_x\right) \tag{2.16}$$

For $B_1 \ll B_0$, the Hamiltonian remains effectively unchanged. An inductor coil, however, can also provide frequency modulated magnetic fields. In NMR, these frequencies are typically in the radio frequency (RF) range. The system Hamiltonian, becomes[21],

$$\mathcal{H} = \frac{-\gamma B_0\sigma_z}{2} - e^{\left(\frac{-\imath(\omega_{rf}t+\phi)\sigma_z}{2}\right)}\frac{\gamma B_1\sigma_x}{2}e^{\left(\frac{\imath(\omega_{rf}t+\phi)\sigma_z}{2}\right)} \tag{2.17}$$

where the second term is defined as the external Hamiltonian $\mathcal{H}_{ext}$. A different picture emerges when the dynamics are described in a frame rotating at the frequency of the applied magnetic field ω_{rf}. The rotating frame density matrix $\widetilde{\rho}$ and Hamiltonian $\mathcal{H}'$ are found by applying a unitary frame change operator U_r,

$$U_r = e^{\frac{\imath}{2}\omega_{rf}\tau\sigma_z} \tag{2.18}$$

$$\widetilde{\rho} = U_r\rho U_r^{-1} \quad \mathcal{H}' = U_r\mathcal{H}U_r^{-1} \tag{2.19}$$

Plugging these quantities into the Liouville-Von Neumann equation yields a time independent effective Hamiltonian $\widetilde{H}$ of

$$\widetilde{\mathcal{H}} = \mathcal{H}' - \frac{\omega_{rf}\sigma_z}{2} = \frac{(\omega_0 - \omega_{rf})}{2}\sigma_z - \frac{\omega_1}{2}\sigma_x \tag{2.20}$$

where the Larmor Frequency and the RF power are defined as $\omega_0 = -\gamma B_0$ and $\omega_1 = -\gamma B_1$ respectively. One should note the resonance condition $\omega_0 = \omega_{rf}$ entirely eliminates the σ_z term in the effective Hamiltonian. The time independence of the rotating frame effective Hamiltonian allows for solution of the output density matrix by Equation 2.14.

2.5 Multiple Qubit Molecules and the Spin-Spin Scalar J coupling

So far, the density matrix and system Hamiltonian has been described for single spin molecules. However, for the purposes of QIP, it is necessary to investigate multi-spin molecules like C-13 labelled Alanine. Figure 2-1 shows a graphical model of the molecule. Here, the three C-13 labelled nuclei are spin 1/2 particles that act as qubits. For a pure state, the N-spin system is represented by a ket with 2^N elements. A mixed state is rep-

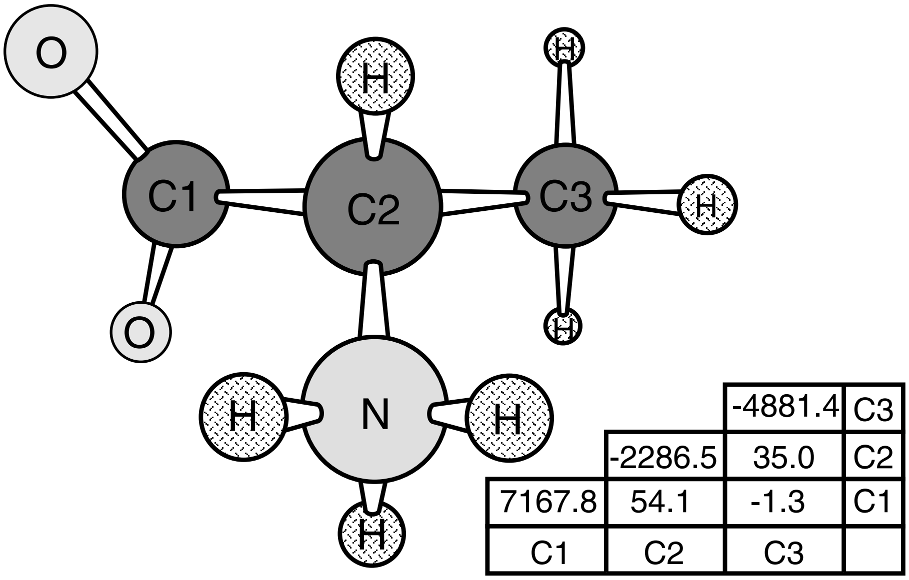

		-4881.4	C3
	-2286.5	35.0	C2
7167.8	54.1	-1.3	C1
C1	C2	C3	

Figure 2-1: A Graphical Representation of the Alanine Molecule. At the bottom right, the chemical shift frequencies and the scalar coupling strengths are shown in units of Hz.

resented by a $2^N \times 2^N$ density matrix. This expanded space is spanned by N Kroenicker products of any of the Pauli spin operators and identity.

Each carbon nuclei acts as a magnetic dipole, and hence the Hamiltonian includes a Zeeman term for each qubit. Each carbon nuclei has the same gyromagnetic ratio, but its surrounding electron clouds shields the nucleus from the static field to different degrees. As a result, each carbon nuclei will experience a unique local magnetic field. In the rotating frame, the sum of the Zeeman terms gives the chemical shift Hamiltonian,

$$\mathcal{H}_{cs} = \sum_{i}^{N} (\omega_{0i} - \omega_{rf})\, \sigma_{zi} \tag{2.21}$$

where the subscript i denotes the spin index. Figure 2-1 shows the chemical shift frequencies of Alanine's three spins. Additionally, the σ_{z1} notation implies two Kroenicker products with identity I_2, I_3, on the second and third spins. The introduction of multiple spin 1/2 particles to a molecule also brings about a spin-spin scalar coupling that acts through electrons of the molecular bonds. Any two spins i and j couple with each other by a constant factor of J_{ij}. The scalar coupling Hamiltonian is,

$$\mathcal{H}_J = \frac{\pi}{2} \sum_{i>j} \sum_{j} J_{ij} \sigma_i \cdot \sigma_j \tag{2.22}$$

The scalar coupling Hamiltonian is usually simplified using weak coupling limit. When the difference in chemical shift frequencies of any two spins $\omega_{0i} - \omega_{0j}$ is much greater than their scalar coupling constant J_{ij}, the $\sigma_{xi} \cdot \sigma_{xj}$ and $\sigma_{yi} \cdot \sigma_{yj}$ become nonsecular. In other words, the $\sigma_{zi} \cdot \sigma_{zj}$ term, because it commutes with the Zeeman Hamiltonian, will have a greater effect on the eigenvalues of the total Hamiltonian [17]. The internal Hamiltonian $\mathcal{H}_{int}$ is then defined as the sum of the chemical shift and weak scalar coupling Hamiltonians.

$$\mathcal{H}_{int} = \sum_{k=1}^{N} (\omega_{0k} - \omega_r f)\, \sigma_{zk} + \frac{\pi}{2} \sum j > k \sum_{k} J_{jk} \sigma_{zj} \sigma_{zk} \tag{2.23}$$

With the Zeeman, scalar coupling, and external Hamiltonians defined, the output density matrix in the rotating frame can be found by Equation 2.14. Transforming back into the lab frame requires the inverse frame change operator, $U_r^{-1} = \exp(-\imath \omega_{rf} \tau \sum_i^N \sigma_{zi}/2)$, and gives the output density matrix in the lab frame,

$$\rho(\tau) = U_r^{-1} e^{-\imath \widetilde{\mathcal{H}} \tau} \rho_{in} e^{\imath \widetilde{\mathcal{H}} \tau} U_r \tag{2.24}$$

This yields the overall unitary evolution operator U_{net}.

$$U_{net} = U_r^{-1} e^{-\imath \widetilde{\mathcal{H}} \tau} \tag{2.25}$$

Once the internal and external Hamiltonians have been well defined, steps can be taken to manipulate their dynamics such that the spin system follows a desired evolution.

Chapter 3

A Method for Compensating for Incoherent Errors

The previous chapter developed the Hamiltonian of a liquid state NMR system, and showed its dependence on the chemical shifts, spin scalar coupling, and the RF power. This chapter will continue by explaining coherent and incoherent errors in quantum control; especially those that arise when this Hamiltonian is experimentally implemented. It will briefly review previous methods of compensation and then will proceed to describe a new general method provided that one has an understanding of the system's dynamics and its incoherent errors.

3.1 Incoherent Errors in Quantum Control

Quantum Information Processing uses a sequence of unitary operations to map a set of input states to a set of output states. Such a quantum algorithm requires a set of universal gates which comprise its building blocks. The physical implementation of an arbitrary algorithm requires a quantum system with a Hamiltonian that has a sufficient number of control parameters such that it allows for the generation of the universal set of gates [22].

Various types of errors occur in the physical implementation of a quantum gate. Given an arbitrary input density matrix ρ_{in}, a quantum gate will map it ideally to a theoretical output density matrix ρ_{th}. Assuming that the transformation is a unitary operation U_{th}, the output density is given by,

$$\rho_{th} = U_{th}\rho_{in}U_{th}^{\dagger} \tag{3.1}$$

In the physical implementation, the input density matrix is mapped instead to ρ_{out} through the unitary operator U_{net}. The projection P of ρ_{out} onto ρ_{th} provides a good metric of the similarity of the two density matrices[24].

$$P = \frac{Tr(\rho_{out}\rho_{th})}{\sqrt{Tr(\rho_{out}^2\rho_{th}^2)}} \tag{3.2}$$

While a measure of the accuracy of the output density matrix is useful, it does not predict its accuracy with respect to a theoretical density matrix for a different input state. Instead, a metric called the gate fidelity, F, is needed. For an N spin system, the fidelity is defined as the average of all of the projections, P_k, for an orthogonal basis of inputs ρ_k,

$$F = \frac{1}{2^{2N}} \sum_{k}^{2^{2N}} P_{\rho_k} \tag{3.3}$$

Fortunato et al. show that this is equivalent to a direct comparison of the ideal theoretical unitary operator and the experimental unitary operator[9].

$$F = \frac{1}{2^{2N}} \left| Tr(U_{th}U_{net}^{\dagger}) \right|^2 \tag{3.4}$$

One should note that the fidelity approaches unity as U_{th} and U_{net} become the same. While perfect control, or a fidelity of one is not required, fault tolerance requires a fidelity of at least 0.9999 to 0.999999 depending on the assumptions used[23].

Coherent errors as well as incoherent errors lower the gate fidelity. Coherent errors arise due to the dissimilarity of two unitary operators. Nevertheless, the physical system as an ensemble, still evolves due to a single net unitary operator. Incoherent errors arise when portions of the ensemble evolve due to separate Krauss operators, A_k. The output density matrix is then given by,

$$\rho_{out} = \sum_k A_k \rho_{in} A_k^{\dagger} \tag{3.5}$$

and the gate fidelity becomes[9],

$$F = \frac{1}{2^{2N}} \sum_k \left| Tr(U_{th}A_k^{\dagger}) \right|^2 \tag{3.6}$$

Incoherent errors are typically divided into temporal and spatial. While this thesis primarily addresses spatial incoherence errors, Section 6.2 will propose extensions to temporal incoherence. A good example of spatial incoherence in liquid state NMR is the RF inhomogeneity. Ideally, the coil will produce a spatially uniform magnetic field with a constant amplitude. In actuality, the RF magnetic field will vary in amplitude across the volume of the sample. The RF field power amplitudes $\alpha_k\omega_1$, weighted by fractions of the volume b_k gives the evolution of the input density matrix.

$$\rho_{out} = \sum_k b_k U_k \rho_{in} U_k^\dagger \tag{3.7}$$

where the Unitary operator U_k is dependent on the RF amplitude;

$$U_k = U_r^{-1} e^{-\imath(H_{int} + \sum_j^N \frac{\alpha_k\omega_1}{2}\sigma_{xj})\tau} \tag{3.8}$$

One should note that Equation 3.7 follows the form of Equation 4.2 when $A_k = \sqrt{b_k}U_k$. Hence, it will cause incoherent errors with respect to a theoretical unitary gate U_{th}.

The degree of these incoherent errors can be described analytically for a single spin system. For an on-resonance pulse ($\omega_o = \omega_{rf}$), the internal Hamiltonian vanishes, and an ideal coil is only capable of producing transformations of the form:

$$U_{th} = e^{-\imath\phi\sigma_z} e^{\frac{-\imath\omega_1\tau\sigma_x}{2}} e^{\imath\phi\sigma_z} \tag{3.9}$$

A non-ideal coil will have Krauss operators of the form,

$$A_k = \sqrt{b_k} e^{-\imath\phi\sigma_z} e^{\frac{-\imath\alpha_k\omega_1 t\sigma_x}{2}} e^{\imath\phi\sigma_z} \tag{3.10}$$

Substituting Equations 4.14 and 4.15 into Equation 4.6 directly yields the fidelity as function of the RF inhomogeneity description.

$$F = \sum_k b_k \cos^2\left[(1-\alpha_k)\omega_1\tau\right] \tag{3.11}$$

Using the above result, a uniform distribution with a width of 10 percent immediately causes the fidelity to drop to 0.99875. This drop is very significant when compared to the fault tolerance threshold. Additionally, one can expect that the error due to RF inhomogeneity would be amplified for coupled systems with multiple spins.

3.2 A Brief Review of Compensation for RF Inhomogeneity

Previous methods in compensating for RF Inhomogeneity have typically used a sequence of pulses that have certain symmetries that to first order average out RF inhomogeneity errors while still achieving the desired control on the spin system. Such ideas are prevalent in a variety of well developed 'echo' methods [25], [26], [27]. Shaka et al proposed a method based upon 90° and $270\circ$ rotations placed sequentially in super-cycles [28]. Finally, an extensive review of composite pulse methods is provided by Levitt [29].

3.3 An Method for Compensation

From Equation 4.5, the compensation problem is defined as finding a set of Krauss operators that give a fidelity that approaches unity for a given theoretical gate U_{th}. Each of the Krauss operators will differ from the others by their dependence on the power density function. Each will also depend on a set of parameters whose values are the same for all of the Krauss operators. In the proposed method, α_k and b_k differentiate the Krauss operators while the four parameters ω_1, ω_{rf}, ϕ, and τ, are constant for each operator. These parameters are chosen for their physical significance in the experimental implementation. No statement is made about whether this is the only or best parameterization. With it, however, the problem reduces to finding optimal values of RF power, frequency, phase and time given a measured set of values α_k and b_k. Prior to starting a robust compensation algorithm, it is necessary to measure the power density function that describe these values.

3.3.1 Experimental Determination of RF Inhomogeneity

The RF inhomogeneity can be determined by measuring the nutation frequency of the NMR signal after a single pulse of variable duration. A molecule with a single carbon-13 labelled spin, Chloroform ($CHCl_3$ was chosen as the sample. A single on resonance pulse $\theta = \omega_1 \tau$ about the x-axis was applied and signal was measured. The RF power was chosen such that its amplitude is much greater than any scalar coupling constants. The pulse was varied in duration and then repeated. Considering only the carbon species, the output density matrix for the l^{th} pulse is,

$$\rho_l = \sigma_z \sum_k \frac{b_k}{2} \cos(\omega_k \tau_l) + \sigma_x \sum_k \frac{b_k}{2} \sin(\omega_k \tau_l) \tag{3.12}$$

and the free induction decay signal is given by

$$S(l,t) = \sum_k \frac{b_k^2}{2} \sin(\omega_k \tau_l) e^{-t/T_2} \tag{3.13}$$

An extra factor of of b_k is acquired because the RF coil is also used as the receiver and has the same sensitivity to detecting magnetic fields as delivering them. In order to maximize signal to noise, the signal is integrated in time. The Fourier transform with respect ω_1 is then taken;

$$S(w) = T_1 \jmath \sum_k b_k^2 \left[\delta(\omega - \omega_{1k}) - \delta(\omega - \omega_{1k})\right] \tag{3.14}$$

This signal describes the density b_k of a given power ω_{1k}. This experiment was performed on a Bruker 300 MHz, as well as a 400 MHz spectrometer. Figure 4-1 shows the experimental results in dimensionless units and normalized to integrate to unity. The RF coil in the 300MHz magnet had a density function width of 6.23 percent at its half maximum. The average power delivered to the sample by this coil was attenuated from the ideal value by 3.50 percent. The 400 MHz magnet had a similar result. Its width and attenuation were 7.00 and 5.64 percent respectively. The RF coils in both magnets also show an asymmetry in the density of powers delivered to the sample. As expected, both show long tails below the ideal power of ω_1. However, a significant portion of the sample is exposed to powers greater than ω_1. This experimental data was then fit with a polynomial regression for powers below the reference and fit with an exponential regression for higher powers. This fit directly gives the power levels $\alpha_k \omega_1$ and their respective fractions b_k, required for the optimization algorithm.

3.3.2 Optimization Algorithm

Once the various power levels and their weighting is found, optimal values of ω_1, ω_{rf}, ϕ and τ can be found using numerical methods. First, a physically implementable initial guess is made for each of the parameters. Specifically, $\omega_1 \epsilon [0, 12]$kHz, $\omega_{rf} \epsilon [-16, 16]$kHz, $\phi \epsilon [0, 2\pi]$, and $\tau \epsilon [30, 600] \mu s$. There exists more than a unique guess that leads to a convergent result.

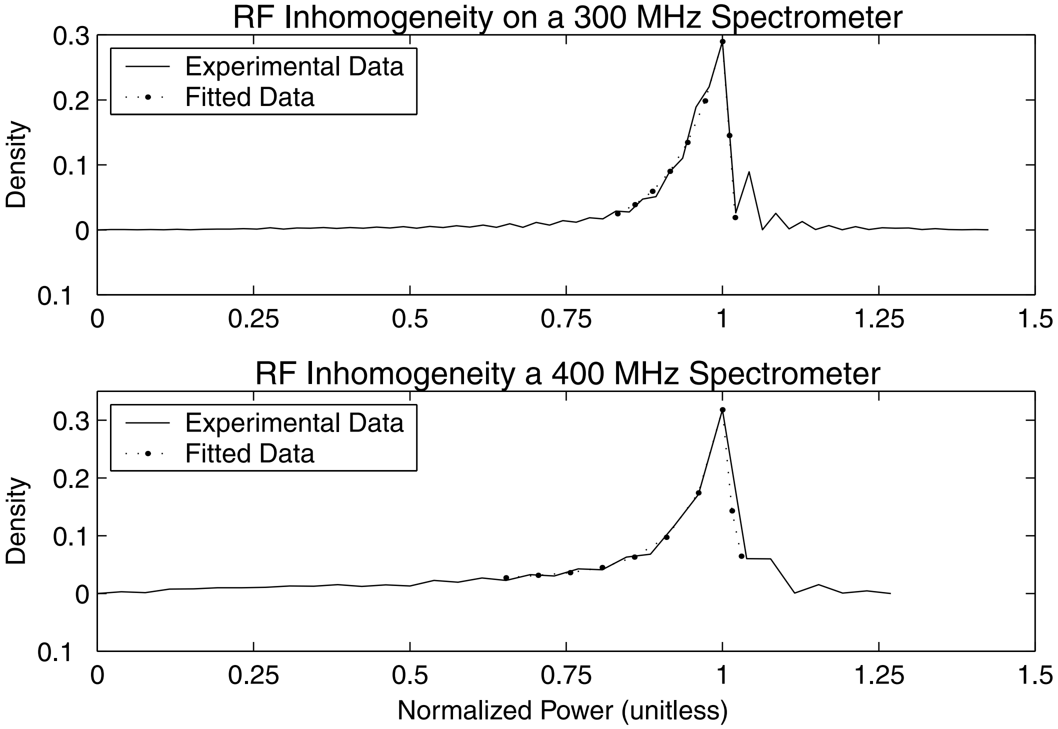

Figure 3-1: On the 300MHz spectrometer, the width of the density function at half the maximum value was 6.23 percent. Similarly, the 400 MHz spectrometer had a width of 7.00 percent. Integrating over the density functions yields an average delivered power attenuated by 3.50 and 5.64 percent respectively.

No guarantee can be made that the algorithm will find the global optima. Instead, different guesses can converge to different optima with nearly equivalent fidelities. Next, the set of Krauss operators associated with these pulses are calculated, the pulse fidelity with respect to a given gate is calculated. A new quantity, χ defined as $\chi = 1 - F$, is then minimized using a Nelder-Mead simplex search. If the optimal parameters do not meet a chosen convergence criterion i.e. $\chi = 0.001$, the pulse duration τ is broken into two separate durations τ_1 and τ_2. Each of these durations will have a power, frequency, phase and duration such that the new search has a total of eight parameters to be optimized. In effect, the algorithm is expanded to find two separate sets of Krauss operators. Equivalently, the RF pulse power, frequency, phase and time become piecewise constant functions in time. This process of adding a new duration with four new parameters is repeated as many times as necessary. Equation 3.7 still determines the output density matrix, and the M sets of Krauss operators can be combined to create a single set of effective Krauss operators.

$$A_k = \sqrt{b_k} \prod_m^M U_{km} \tag{3.15}$$

where U_{km} is defined by Equation 3.8 and ω_1, ω_{rf}, ϕ and τ are dependent on the duration index m. Figure 4-2 shows how an initial guess of constant RF pulse parameters becomes a set of piecewise constant time dependent parameters developed for a 180° rotation on Alanine's first spin.

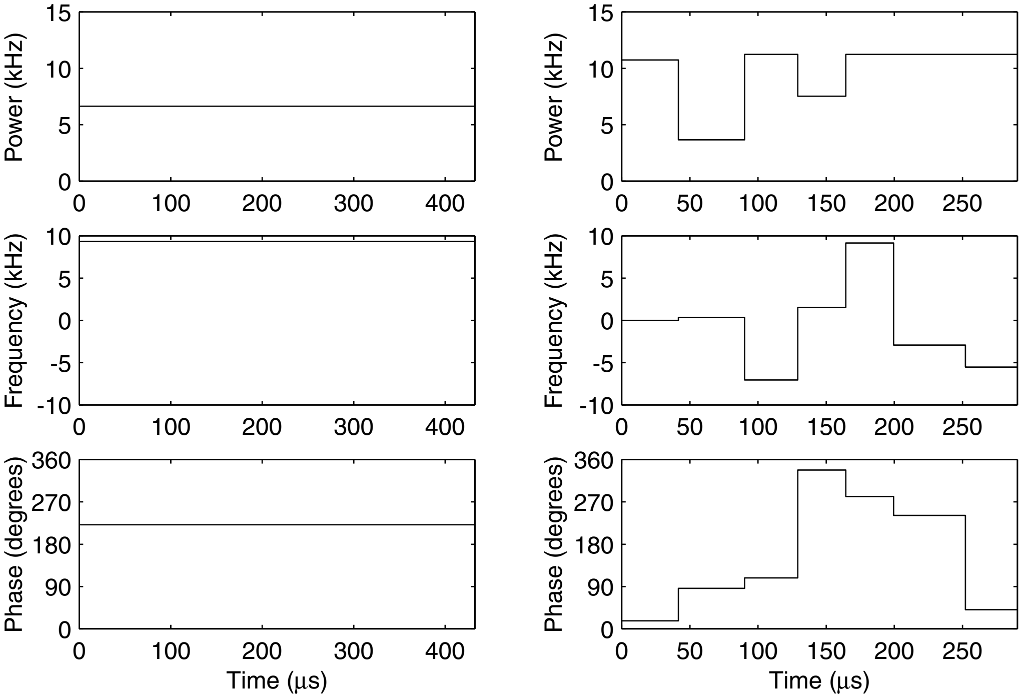

Figure 3-2: On the left is a an initial guess of the optimization parameters. On the right is the end result of the optimization algorithm; a set of piecewise constant time dependent parameters that gives a 180° rotation on Alanine's first spin.

In the minimization routine, the optimal parameters must remain within a physically implementable search space defined previously in the creation of the initial guess. To ensure a feasible solution, the search is constrained by adding to the chi function functions that penalize non-feasible value of the parameters. Specifically,

$$\chi = 1 - F + \chi_{\omega_1} + \chi_{\omega_{rf}} + \chi_\tau \tag{3.16}$$

where χ_{ω_1}, $\chi_{\omega_{rf}}$, and χ_{τ} are penalty functions that depend on each of the parameters respectively. These functions are nearly flat in the feasible region and are sharply increasing at the regions' boundaries. Many types of smooth functions can be used while still retaining convergence. Figure 4-3 shows the shape of the functions used in this study. The power penalty function used is,

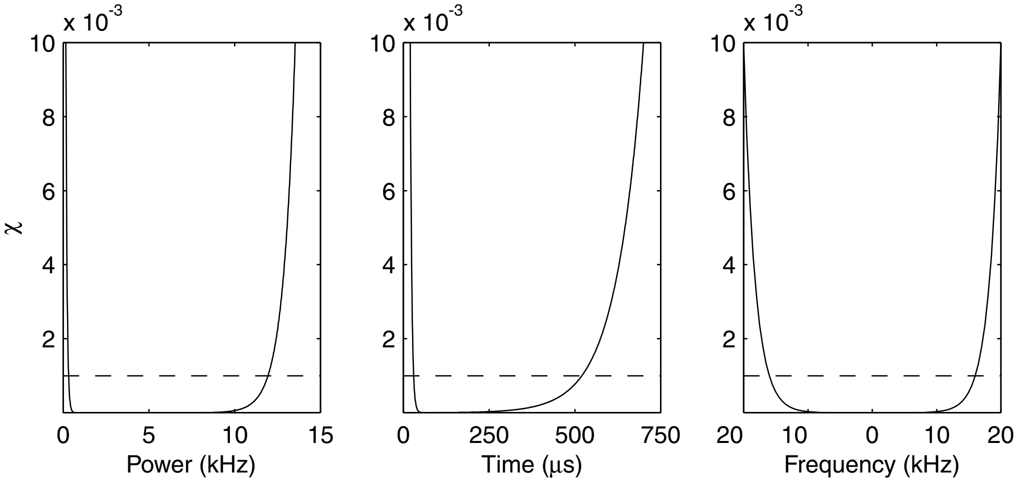

Figure 3-3: The three penalty functions for the pulse power, time and frequency. Negative powers, powers greater than 12kHz, and frequencies greater than 16kHz are strongly penalized. Transient errors are lessened by penalizing durations shorter than $30\mu s$. Otherwise, preference is given to shorter duration pulses.

$$\chi_{\omega_1} = e^{\left(-2.3026\times10^{-3}\min(\omega_1(t))\right)} + \left(3.1623*10^{-10}\right) e^{\left(2.3026*10^{-4}\max(\omega_1(t))\right)} \tag{3.17}$$

An exponentially increasing penalty prevents negative powers for the duration of the pulse. Similarly, the second prevents high powers that are capable of "arching" or "heating" the coil. The time penalty function is,

$$\chi_{\tau} = 10e^{\left(-2.3026*10^{5}\min(\tau_n)\right)} + \left(1.2916*10^{-5}\right) e^{\left(+1.2792*10^{4}\tau\right)} \tag{3.18}$$

The first term prevents any set of parameters from being applied for too short of a time period. In this case, periods shorter than $30\mu s$ will have errors dominated by transients in the experimental implementation. The second term in the penalty function is a less steep exponential. Here the function has two purposes. It eliminates pulses longer than $500\mu s$, and gives preference to pulses of shorter total duration. Long pulses, especially when used in sequences) are prone to decoherent errors such as relaxation [17]. Lastly, the frequency penalty function is,

$$\chi_{\omega_{rf}} = 10^{-6} e^{\left(9.1617*10^{-5}|max(\omega_{rf}(t))|\right)} \tag{3.19}$$

Here negative frequencies are allowed, but more importantly the magnitude of the frequency is limited to 16. The RF frequency must remain within the bandwidth capabilities of the spectrometer.

3.4 Summary of Pulse Parameters

The above algorithm was used to make a set of 11 robust pulses that each implement a given theoretical unitary gate. Also, the same algorithm was used to make 'normal' pulses; i.e. pulses that did not compensate for incoherent errors in the calculation of the fidelity. The parameters for robust pulses can be found in Appendix B while uncompensated pulse parameters can be found in C. The uncompensated pulses had an average duration of 236.49 μs. This time was usually broken into four shorter durations; while some pulses had as few as three constant durations and as many as seven durations. These pulses on average had a maximum power of 8.7255 kHz; while highest power pulses had a power of 10.77kHz. The compensated pulses were on significantly longer; lasting on average 341.99 μs. This is, however, much shorter than conventional methods of creating single spin rotations. Qualitatively, the biggest difference in the two sets of pulses. The robust pulses as a set required on average seven constant durations with a minimum of six durations and a maximum of 12. The maximum power numbers were also higher, but not as significantly. On average, the maximum power was 10.70kHz, and the most powerful pulse required 11.3kHz.

3.5 Simulated Robustness to RF Inhomogeneity

The robustness of the two sets of the pulses can also be directly compared in simulation. Here robustness is defined as the ability for a particular pulse to maintain fidelity as systematic errors are introduced. For this simulation of robustness, the width of the RF power density function at half amplitude was scaled by a constant factor and the resulting fidelity was calculated. Figure 3-4 shows the performance of the two sets of eleven pulses. For the

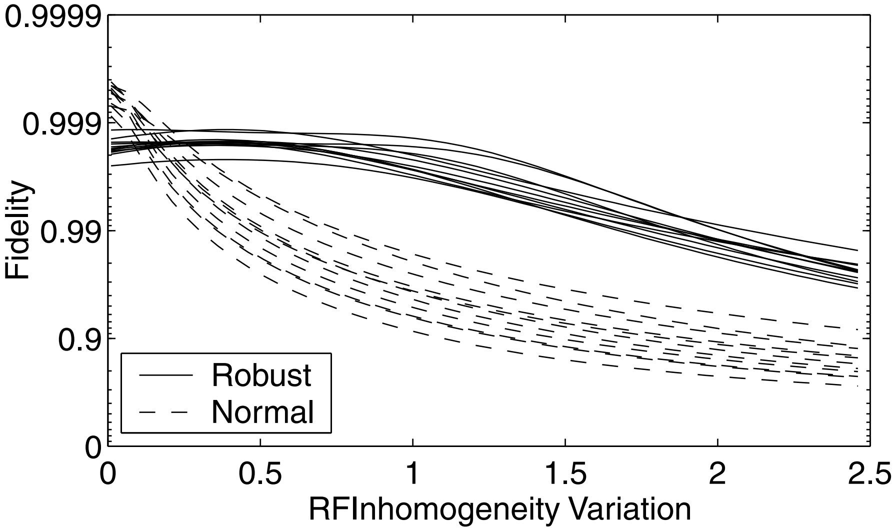

Figure 3-4: The fidelity performance as logarithmic distance to unity is shown for 11 robust and 11 uncompensated pulses as the width of RF power density function is scaled by a constant factor. The robust pulses show a greater ability to maintain fidelity as greater RF inhomogeneity is introduced.

experimentally measured inhomogeneity, the robust pulses out perform the uncompensated pulses by an order of magnitude. Additionally, they have a nearly constant fidelity for more ideal RF coils. The uncompensated pulses, however, show a steep degradation as RF inhomogeneity is introduced, and only show high performance for nearly ideal coils. At RF inhomogeneities greater than the ones experimentally measured, the uncompensated pulses degrade at a slower, but still nearly exponential rate. This rate is approximately the same for both sets of pulses for very large RF inhomogeneities. It is not clear why the robust pulses's performance begins to degrade significantly after the introduction of RF inhomogeneity strengths greater than the one experimentally measured. Two possible explanations exist. The algorithm can be compensating fully for the errors used as its input. In which case, finding new pulses for an RF coil with a different power density function will show a break point in the performance at that power density function's width. On the other hand, the performance break point can be a function of the internal dynamics of the molecule. In that case, the performance break point will be fixed at the current width of approximately 6.23 percent. It is likely that both explanations contribute, and this question can be investigated further by making pulses for a variety of different RF inhomogeneity strengths.

These simulated results suggest that the proposed algorithm is capable of finding a set of parameters such that the density matrix's evolution will closely correspond to the desired unitary gate. Additionally, they show that the robust pulses will out perform the uncompensated pulses when they are experimentally implemented and are in the presence of incoherent evolutions.

Chapter 4

Robust Compensation for Incoherent Errors

The advent of QIP and its restrictions for fault tolerance have necessitated stricter requirements on the precision of quantum control. Improvement in precision has typically been divided into the elimination of coherent, incoherent and decoherent errors. Various techniques have been developed to lessen coherent errors REF(somedudes). Other techniques lessen incoherent errors but often have the disadvantages of longer pulse times and lower pulse powers REF(somedudes). With a previous understanding of the incoherent errors it is possible to achieve greater compensation while still using high power and short duration pulses.

4.1 Gate Fidelity as a Control Metric

Before focusing on a compensation method, it is necessary to define a control metric that appropriately describes the precision of the control. It should reflect coherent, as well as incoherent errors, and also be experimentally accessible. The gate fidelity, F, defined by !!Fortunato et al!! provides such a metric REF(1st control paper).

Given an input state ρ_{in} that evolves due to an arbitrary theoretical unitary operator U_{th}, the ideal output state is given by,

$$\rho_{th} = U_{th} \rho_{in} U_{th}^{\dagger} \tag{4.1}$$

Similarly, in the physical implementation, the input density matrix maps to ρ_{out} through the unitary operator U_{net}. Allowing incoherent errors in the experimental implementation causes ρ_{out} to have a non-unitary evolution described by a sum of Krauss operators A_k.

$$\rho_{out} = \sum_k A_k \rho_{in} A_k^\dagger \tag{4.2}$$

The projection P, describes the degree of similarity of the output states.

$$P = \frac{Tr(\rho_{out}\rho_{th})}{\sqrt{(\rho_{out}^2)(\rho_{th}^2)}} \tag{4.3}$$

While the projection is experimentally accessible, it does not predict the degree of control for another input state. For an N spin system, the gate fidelity does this by averaging all the projections using a basis of inputs ρ_k.

$$F = \frac{1}{2^N} \sum_k^{2^N} P_{\rho_k} \tag{4.4}$$

!Fortunato et al! show this expression reduces to a function of just the theoretical unitary operator U_{th} and the Krauss operators A_k REF(1st control paper).

$$F = \frac{1}{2^{2N}} \sum_k \left| Tr(U_{th} A_k^\dagger) \right|^2 \tag{4.5}$$

One should note that in the case of a unitary experimental evolution the fidelity reduces to,

$$F = \frac{1}{2^{2N}} \left| Tr(U_{th} U_{net}^\dagger) \right|^2 \tag{4.6}$$

4.2 NMR RF Inhomogeneity as an Example of an Incoherent Error

Spatial inhomogeneity in the amplitude of the RF magnetic field provides a good example of incoherent errors caused by non-unitary evolution. The NMR spin system evolves due to a sum of interactions; a zeeman interaction due to a large static magnetic field, a spin-spin scalar coupling, and finally RF pulses that are used to control the system. The first two interactions comprise the internal Hamiltonian. In terms of Pauli spin operators, and assuming weak coupling,

$$\mathcal{H}_{int} = \sum_{i}^{N} \frac{\omega_{oi}}{2}\sigma_{zi} + \sum_{i>j}^{N}\sum_{j}^{N} \frac{J_{ij}}{2}\sigma_{zi}\sigma_{zj} \tag{4.7}$$

where ω_{oi} is the chemical shift frequency and J_{ij} is the spin-spin scalar coupling constant.

For a spatially homogenous RF field, the external Hamiltonian describing the interaction of the oscillating RF with the spins is,

$$\mathcal{H}_{ext} = \sum_{i}^{N} e^{\left(\frac{-\imath(\omega_{rf}t+\phi)\sigma_{zi}}{2}\right)} \frac{\omega_1 \sigma_{xi}}{2} e^{\left(\frac{\imath(\omega_{rf}t+\phi)\sigma_{zi}}{2}\right)} \tag{4.8}$$

where ω_{rf} is the RF transmitter frequency, ω_1 is the RF power, and ϕ is the RF phase. For a constant RF power, the total Hamiltonian $\mathcal{H}_{tot} = \mathcal{H}_{int} + \mathcal{H}_{ext}$ can be made time independent by transforming into the frame rotating at the transmitter frequency. The solution to the Liouville-von Neumann equation is,

$$\widetilde{\rho}(\tau) = e^{-\imath\widetilde{\mathcal{H}}\tau}\widetilde{\rho}_{in}e^{\imath\widetilde{\mathcal{H}}\tau} \tag{4.9}$$

where $\widetilde{\rho}$ and $\widetilde{\mathcal{H}}$ are the density matrix and the effective hamiltonian in the new frame. Transforming back into the lab frame requires the inverse frame change operator, $U_r^{-1} = \sum_i^N \exp\left(-\imath(\omega_{rf}\tau + \phi)\sigma_{zi}/2\right)$ and gives the output density matrix in the lab frame.

$$\rho(\tau) = U_r^{-1}e^{-\imath\widetilde{\mathcal{H}}\tau}\rho_{in}e^{\imath\widetilde{\mathcal{H}}\tau}U_r \tag{4.10}$$

This yields the overall unitary evolution operator U_{net}.

$$U_{net} = U_r^{-1}e^{-\imath\widetilde{\mathcal{H}}\tau} \tag{4.11}$$

For a spatially inhomogeneous field, it is necessary to introduce a power density function sufficiently discretized into fractions of a the liquid state sample b_k that are exposed to given RF powers $\alpha_k\omega_1$. Each fraction will evolve independently due to this RF power. The output density matrix becomes,

$$\rho(\tau) = \sum_k b_k U_k \rho_{in} U_k^{\dagger} \tag{4.12}$$

where,

$$U_k = U_r^{-1} e^{-\imath\left(\widetilde{\mathcal{H}}_{int}+\frac{\alpha_k\omega_1}{2}\sum_i^N \sigma_{xi}\right)\tau} \tag{4.13}$$

One should note that when $A_k = \sqrt{b_k}U_k$, the description of RF inhomogeneity found in Equation 4.12 is equivalent to the non-unitary evolution found in Equation 4.2. Hence, it will cause incoherent errors with respect to a theoretical unitary gate U_{th}.

The degree of these incoherent errors can be described analytically for a single spin system. For an on-resonance pulse $(\omega_{o1}) = \omega_{rf}$, the internal Hamiltonian vanishes, an ideal coil is only capable of producing transformations of the form:

$$U_{th} = e^{-\imath\phi\sigma_z} e^{\frac{-\imath\omega_1 t\sigma_x}{2}} e^{\imath\phi\sigma_z} \tag{4.14}$$

A non-ideal coil will have Krauss operators of the form,

$$A_k = \sqrt{b_k} e^{-\imath\phi\sigma_z} e^{\frac{-\imath\alpha_k\omega_1 t\sigma_x}{2}} e^{\imath\phi\sigma_z} \tag{4.15}$$

Substituting Equations 4.14 and 4.15 into Equation 4.6 directly yields the fidelity as function of the RF inhomogeneity description.

$$F = \sum_k b_k \cos^2\left[(1-\alpha_k)\omega_1\tau\right] \tag{4.16}$$

Using the above result, a uniform distribution with a width of 10 percent immediately causes the fidelity to drop to 0.99875. This drop is very significant when compared to the fault tolerance threshold. Additionally, one can expect that the error due to RF inhomogeneity would be amplified for coupled systems with multiple spins.

4.3 An Algorithm for Compensation

From Equation 4.5, the compensation problem is defined as finding a set of Krauss operators that give a fidelity that approaches unity for a given theoretical gate U_{th}. Each of the Krauss operators will differ from the others by their dependence on the power density function. Each will also depend on a set of parameters whose values are the same for all of the Krauss operators. In the proposed method, α_k and b_k differentiate the Krauss operators while the four parameters ω_1, ω_{rf}, ϕ, and τ, are constant for each operator. These parameters are chosen for their physical significance in the experimental implementation. No statement is made about whether this is the only or best parameterization. With it, however, the problem reduces to finding optimal values of RF power, frequency, phase and time given a measured set of values α_k and b_k. Prior to starting a robust compensation algorithm, it is necessary to measure the power density function that describe these values.

4.3.1 Experimental Determination of RF Inhomogeneity

The RF inhomogeneity can be determined by measuring the nutation frequency of the NMR signal after a single pulse of variable duration. A molecule with a single carbon-13 labelled spin, Chloroform ($CHCl_3$ was chosen as the sample. A single on resonance pulse $\theta = \omega_1 \tau$ about the x-axis was applied and signal was measured. The RF power was chosen such that its amplitude is much greater than any scalar coupling constants. The pulse was varied in duration and then repeated. Considering only the carbon species, the output density matrix for the l^{th} pulse is,

$$\rho_l = \sigma_z \sum_k \frac{b_k}{2} \cos(\omega_k \tau_l) + \sigma_x \sum_k \frac{b_k}{2} \sin(\omega_k \tau_l) \tag{4.17}$$

and the free induction decay signal is given by

$$S(l,t) = \sum_k \frac{b_k^2}{2} \sin(\omega_k \tau_l) e^{-t/T_2} \tag{4.18}$$

An extra factor of of b_k is acquired because the RF coil is also used as the receiver and has the same sensitivity to detecting magnetic fields as delivering them. In order to maximize signal to noise, the signal is integrated in time. The Fourier transform with respect ω_1 is then taken;

$$S(w) = T_1 \jmath \sum_k b_k^2 \left[\delta(\omega - \omega_{1k}) - \delta(\omega - \omega_{1k})\right] \tag{4.19}$$

This signal describes the density b_k of a given power ω_{1k}. This experiment was performed on a Bruker 300 MHz, as well as a 400 MHz spectrometer. Figure 4-1 shows the experimental results in dimensionless units and normalized to integrate to unity. The RF coil in the 300MHz magnet had a density function width of 6.23 percent at its half maximum. The average power delivered to the sample by this coil was attenuated from the ideal value by 3.50 percent. The 400 MHz magnet had a similar result. Its width and attenuation were

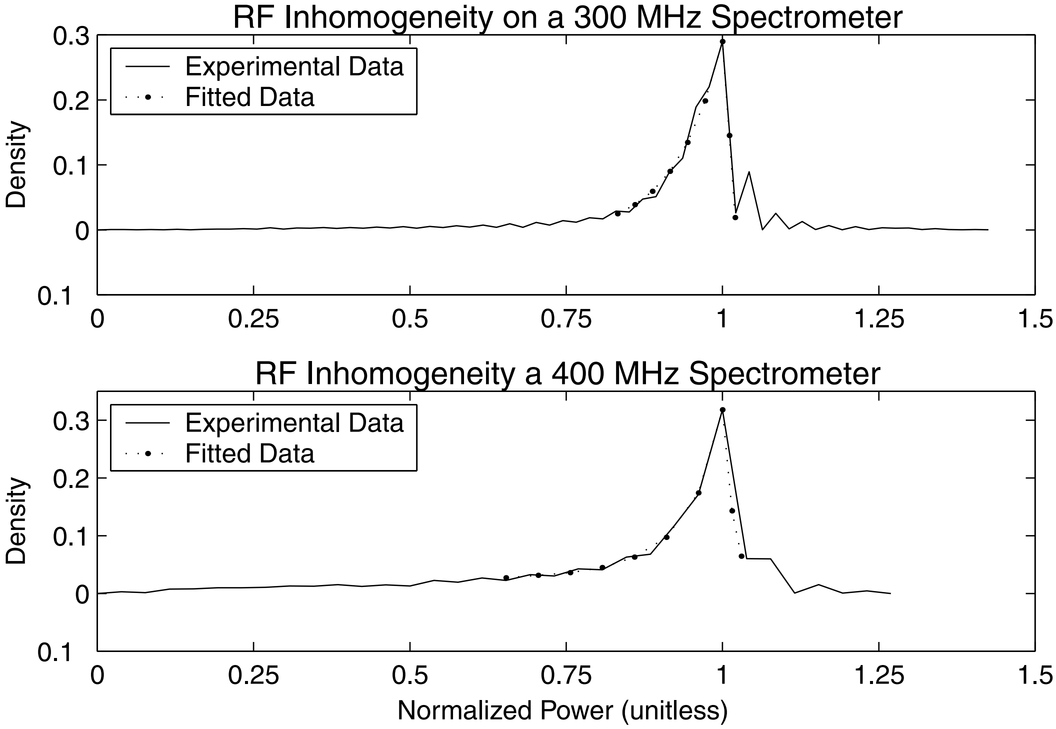

Figure 4-1: On the 300MHz spectrometer, the width of the density function at half the maximum value was 6.23 percent. Similarly, the 400 MHz spectrometer had a width of 7.00 percent. Integrating over the density functions yields an average delivered power attenuated by 3.50 and 5.64 percent respectively.

7.00 and 5.64 percent respectively. The RF coils in both magnets also show an asymmetry in the density of powers delivered to the sample. As expected, both show long tails below the ideal power of ω_1. However, a significant portion of the sample is exposed to powers greater than ω_1. This experimental data was then fit with a polynomial regression for powers below the reference and fit with an exponential regression for higher powers. This fit directly gives the power levels $\alpha_k\omega_1$ and their respective fractions b_k, required for the optimization algorithm.

4.3.2 Optimization Algorithm

Once the various power levels and their weighting is found, optimal values of ω_1, ω_{rf}, ϕ and τ can be found using numerical methods. First, a physically implementable initial guess is made for each of the parameters. Specifically, $\omega_1 \epsilon [0, 12]$kHz, $\omega_{rf} \epsilon [-16, 16]$kHz, $\phi \epsilon [0, 2\pi]$, and $\tau \epsilon [30, 600] \mu s$. There exists more than a unique guess that leads to a convergent result.

No guarantee can be made that the algorithm will find the global optima. Instead, different guesses can converge to different optima with nearly equivalent fidelities. Next, the set of Krauss operators associated with these pulses are calculated, the pulse fidelity with respect to a given gate is calculated. A new quantity, χ defined as $\chi = 1 - F$, is then minimized using a Nelder-Mead simplex search. If the optimal parameters do not meet a chosen convergence criterion i.e. $\chi = 0.001$, the pulse duration τ is broken into two separate durations τ_1 and τ_2. Each of these durations will have a power, frequency, phase and duration such that the new search has a total of eight parameters to be optimized. In effect, the algorithm is expanded to find two separate sets of Krauss operators. Equivalently, the RF pulse power, frequency, phase and time become piecewise constant functions in time. This process of adding a new duration with four new parameters is repeated as many times as necessary. Equation 3.7 still determines the output density matrix, and the M sets of Krauss operators can be combined to create a single set of effective Krauss operators.

$$A_k = \sqrt{b_k} \prod_{m}^{M} U_{km} \tag{4.20}$$

where U_{km} is defined by Equation 3.8 and ω_1, ω_{rf}, ϕ and τ are dependent on the duration index m. Figure 4-2 shows how an initial guess of constant RF pulse parameters becomes a set of piecewise constant time dependent parameters developed for a 180° rotation on Alanine's first spin.

In the minimization routine, the optimal parameters must remain within a physically implementable search space defined previously in the creation of the initial guess. To ensure a feasible solution, the search is constrained by adding to the chi function functions that penalize non-feasible value of the parameters. Specifically,

$$\chi = 1 - F + \chi_{\omega_1} + \chi_{\omega_{rf}} + \chi_{\tau} \tag{4.21}$$

where χ_{ω_1}, $\chi_{\omega_{rf}}$, and χ_{τ} are penalty functions that depend on each of the parameters respectively. These functions are nearly flat in the feasible region and are sharply increasing at the regions' boundaries. Many types of smooth functions can be used while still retaining convergence. Figure 4-3 shows the shape of the functions used in this study. The power

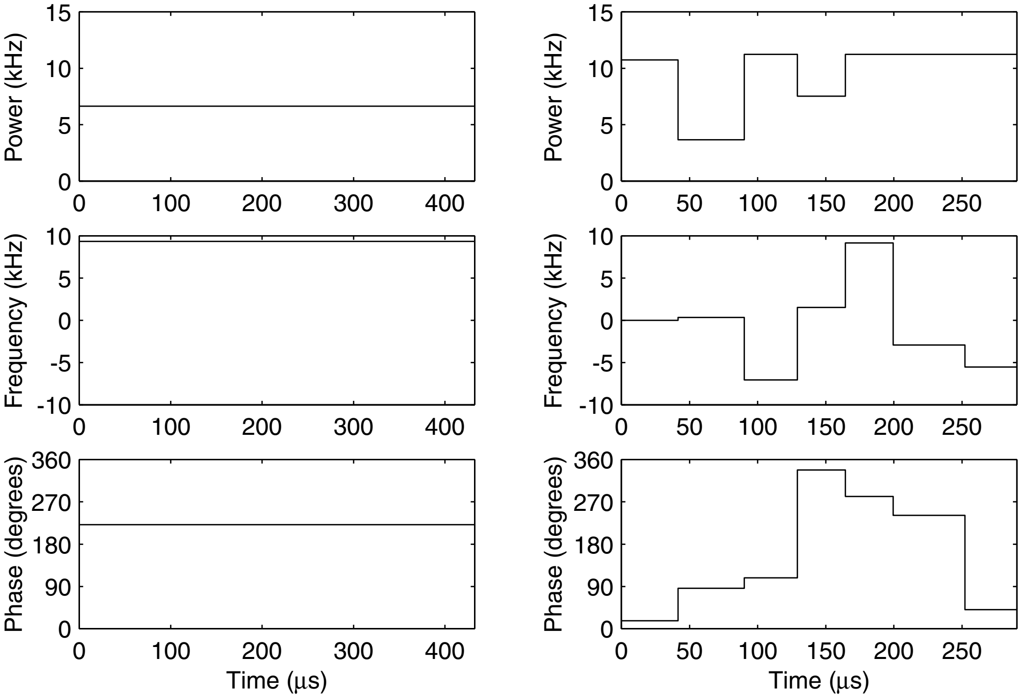

Figure 4-2: On the left is a an initial guess of the optimization parameters. On the right is the end result of the optimization algorithm; a set of piecewise constant time dependent parameters that gives a 180° rotation on Alanine's first spin.

penalty function used is,

$$\chi_{\omega_1} = e^{\left(-2.3026\times 10^{-3}\min(\omega_1(t))\right)} + \left(3.1623 * 10^{-10}\right) e^{\left(2.3026*10^{-4}\max(\omega_1(t))\right)} \tag{4.22}$$

An exponentially increasing penalty prevents negative powers for the duration of the pulse. Similarly, the second prevents high powers that are capable of "arching" or "heating" the coil. The time penalty function is,

$$\chi_{\tau} = 10e^{\left(-2.3026*10^{5}\min(\tau_n)\right)} + \left(1.2916 * 10^{-5}\right) e^{\left(+1.2792*10^{4}\tau\right)} \tag{4.23}$$

The first term prevents any set of parameters from being applied for too short of a time period. In this case, periods shorter than $30\mu s$ will have errors dominated by transients in the experimental implementation. The second term in the penalty function is a less steep exponential. Here the function has two purposes. It eliminates pulses longer than $500\mu s$, and gives preference to pulses of shorter total duration. Long pulses, especially when used

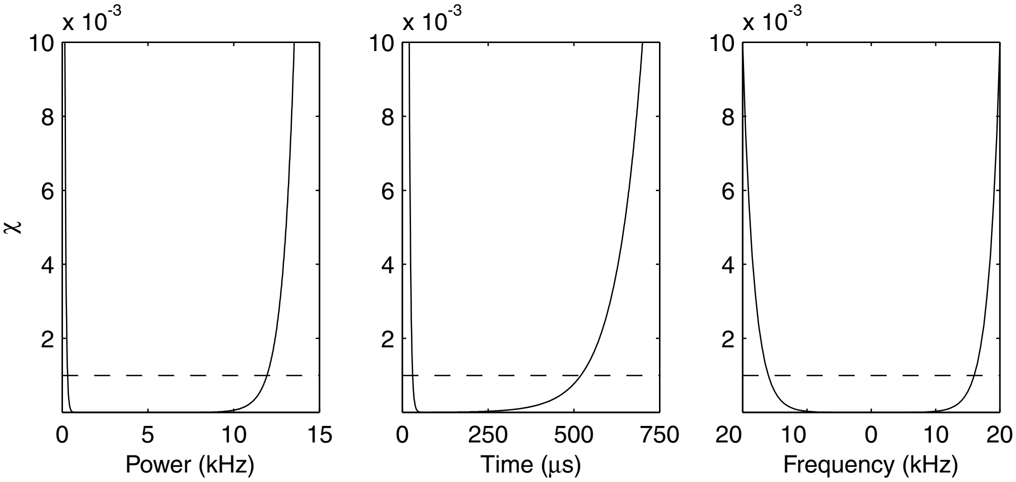

Figure 4-3: The three penalty functions for the pulse power, time and frequency. Negative powers, powers greater than 12kHz, and frequencies greater than 16kHz are strongly penalized. Transient errors are lessened by penalizing durations shorter than $30\mu s$. Otherwise, preference is given to shorter duration pulses.

in sequences) are prone to decoherent errors such as relaxation [17]. Lastly, the frequency penalty function is,

$$\chi_{\omega_{rf}} = 10^{-6} e^{\left(9.1617*10^{-5}|max(\omega_{rf}(t))|\right)} \tag{4.24}$$

Here negative frequencies are allowed, but more importantly the magnitude of the frequency is limited to 16. The RF frequency must remain within the bandwidth capabilities of the spectrometer.

4.4 Exploring Achievable Fidelities

The proposed algorithm shows a good way of finding optimal RF pulse parameters in the presence of incoherent errors. Additionally, it can be repeatedly used to understand the depth and frequency of optimal points in the search space. Specifically, pulses can be found as the search constraints are relaxed and tightened; thereby simulating this method's achievable limits of control using a variety of equipment. A perfectly homogenous coil was assumed and the a set of parameter guesses was made using all of the previously mentioned intervals. While varying the second term in the power penalty function, these guesses were used to find pulses that implement a 90 degree rotation on Alanine's second carbon spin.

Effectively, the upper limit on allowed powers was varied. Figure 6-2 shows the maximum fidelities of these pulses as a function of their maximum power. A total of 2088, 1222, and 599 pulses were made for 300, 600, and 800 MHz magnets respectively. While this method does not ensure finding globally optimal fidelities, the maximal fidelity among many local maxima provides an approximation of the maximum fidelity envelope in the absence of an analytical result. The dotted vertical lines show the minimum chemical shift difference for alanine on 300, 600 and 800 MHz magnets. The achievable fidelities drop dramatically in a low power regime defined by alanine's minimum chemical difference. For this molecule's high power regime, this algorithm is theoretically capable of achieving fidelities of at least 0.999. It appears that increasingly better fidelities can be achieved when a number of durations with increasingly loose power restrictions are used. Finally, significantly better fidelities were found for higher fields. As the static magnetic field strength is increased, the chemical shift differences increase with respect to the constant scalar coupling leading to a greater ability to make selective rotations. For an 800 MHz magnet, theoretical fidelities greater than 0.9999 were achieved. This is the degree of precision required for some estimates of

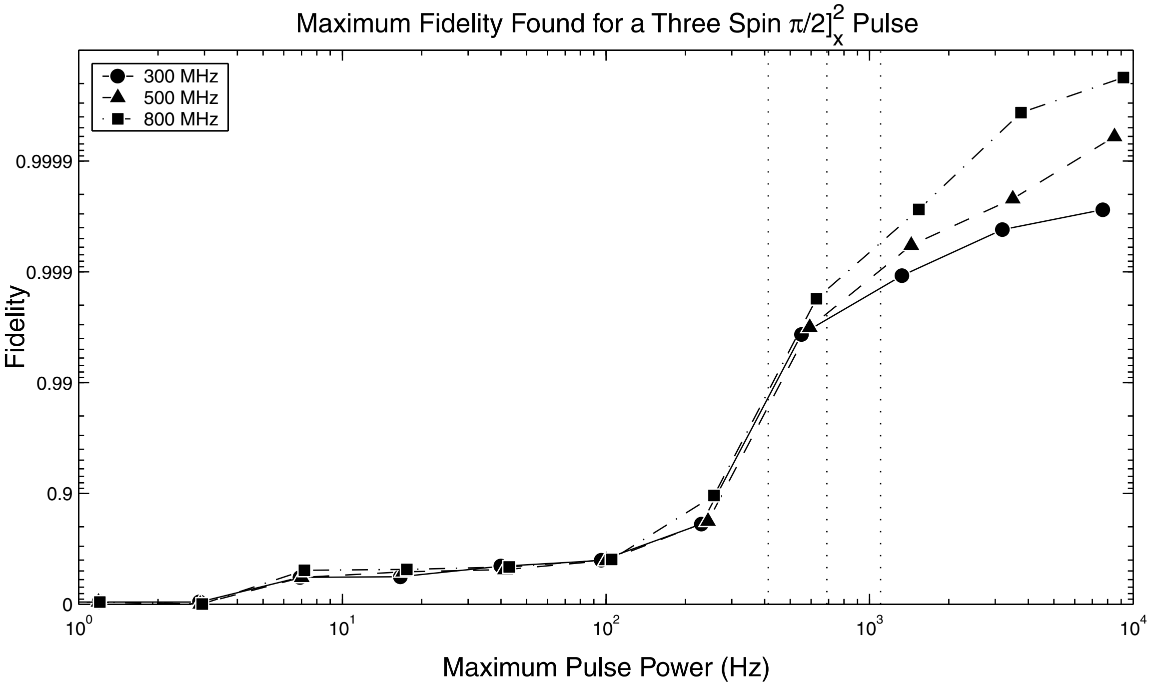

Figure 4-4: Maximum Fidelities found as function of Maximum Power.High fidelity pulses were found in high power regime defined by the minimum chemical shift difference.

fault tolerance.

Chapter 5

Experimental Results

Chapter 3 described the coherent and incoherent errors that arise when experimentally implementing theoretical unitary gates. It went on to provide an algorithm that finds a set of pulse parameters such that the evolution in experiment has minimal coherent errors and is robust towards incoherent errors. This chapter will discuss how these parameters can be realized experimentally. It will then measure the performance of experimental gates with respect to the theoretical ones.

5.1 Experimental Realization of Waveform

Figure 4-2 shows that a given pulse is defined by a set of piecewise time dependent parameters. The difficulty with this is that these functions are not differentiable throughout their whole duration; specifically at the boundaries of any two durations. Real physical systems such as inductor coils follow ordinary diffential equations are not capable of instantaneous changes in their time response. Because the gate fidelity is tuned to these pulse parameters, any experimental derivation from them will introduce experimental errors.

In order to eliminate errors due to waveform distortion, a feedback method was used. (Throughout, this thesis the RF coil has been referred to as a single entity. In actuality, there are two coils; one to excite hydrogen nuclei and the other to excite carbon nuclei.) The robust pulses were digitized and then run on the carbon channel. Meanwhile a digital measurement of the applied magnetic field was made using the Hydrogen coil. The difference between the measured pulse and the desired pulse was then used to create a corrected digital waveform. This feedback process was iterated between four and six times such that the new corrected waveform closely matched the desired pulse found by the algorithm. Figure 5-1 shows a comparison of the desired, uncorrected and corrected waveforms further details of this method can be found at [30]

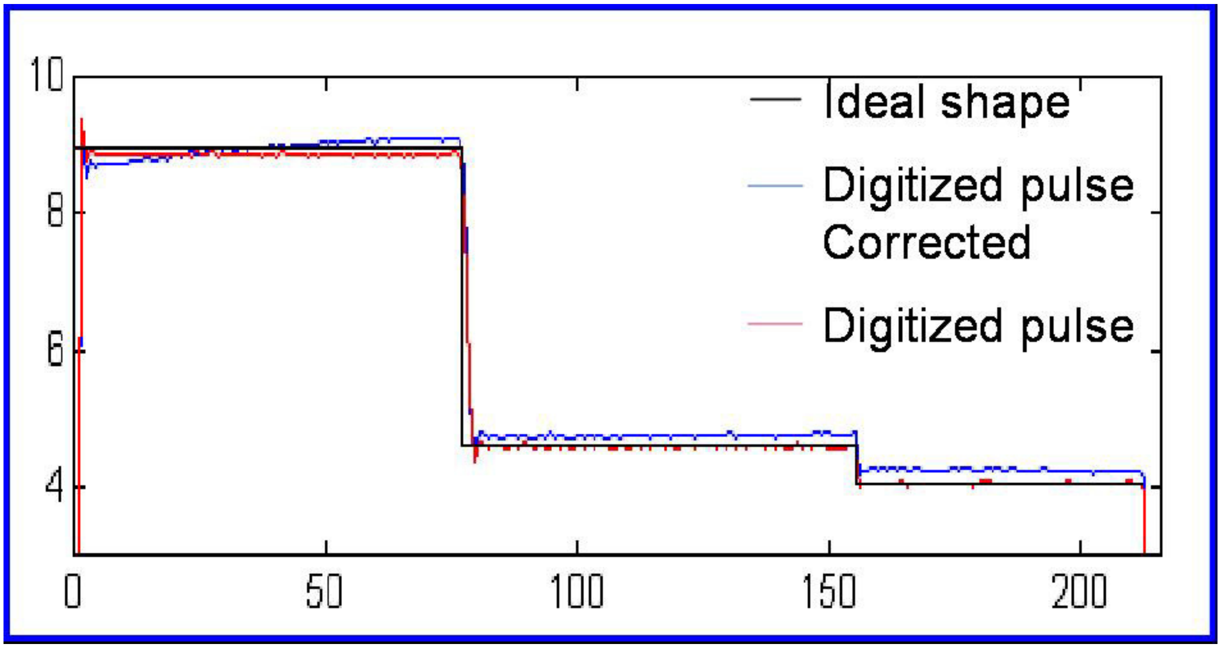

Figure 5-1: A feedback method of realizing the desired robust pulse. The desired pulse requires a set of step functions. The uncorrected waveform shows transient and steady state errors. The corrected waveform more closely tracks the desired waveform.

5.2 State and Process Tomography

Once the preparation steps have been taken to implement the pulse parameters, the experiment can be performed. However, as will all quantum mechanical systems special care must be taken to make the proper measurements. The goals is to extract the experimental fidelity for a given set of pulse parameters. This requires a method called Quantum Process Tomography (QPT) [31]. By Equation 4.4, 2^{2N} states needed to be prepared for each experiment to be done. This is difficult, but is further complicated by the fact that the output density matrix can not be acquired in a single measurement. In NMR only single quantum coherence product operators are observable [17]. In other words, the NMR signal only provides the time dependent coefficients to the observable product operators. For a three spin system like Alanine, the 24 observables are,

$$\begin{array}{cccccccc} \sigma_{x1} & \sigma_{x1}\sigma_{z2} & \sigma_{x1}\sigma_{z3} & \sigma_{x1}\sigma_{z2}\sigma_{z3} & \sigma_{y1} & \sigma_{y1}\sigma_{z2} & \sigma_{y1}\sigma_{z3} & \sigma_{y1}\sigma_{z2}\sigma_{z3} \\ \sigma_{x2} & \sigma_{z1}\sigma_{x2} & \sigma_{x2}\sigma_{z3} & \sigma_{z1}\sigma_{x2}\sigma_{z3} & \sigma_{y2} & \sigma_{z1}\sigma_{y2} & \sigma_{y2}\sigma_{z3} & \sigma_{z1}\sigma_{y2}\sigma_{z3} \\ \sigma_{x3} & \sigma_{z1}\sigma_{x3} & \sigma_{z2}\sigma_{x3} & \sigma_{z1}\sigma_{z2}\sigma_{x3} & \sigma_{y3} & \sigma_{z1}\sigma_{y3} & \sigma_{z2}\sigma_{y3} & \sigma_{z1}\sigma_{z2}\sigma_{y3} \end{array} \tag{5.1}$$

In order to obtain the coefficients of the product operators, QPT requires another method called quantum state tomography [31]. This process is done by applying 'read out' pulses that rotate non-observable product operators to observables. Figure 5-2 gives a conceptual diagram of the entire process of QPT. An infinite number of different sets of read out pulses yield all the product operators, but the following set of 8 $\frac{\pi}{2}$ pulses is sufficient.

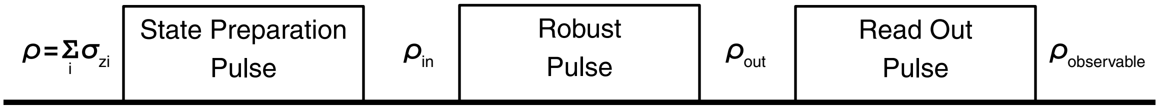

Figure 5-2: On the left is a an initial guess of the optimization parameters. On the right is the end result of the optimization algorithm; a set of piecewise constant time dependent parameters that gives a 180° rotation on Alanine's first spin.

$$I \quad \tfrac{\pi}{2}\big|_x^1 \quad \tfrac{\pi}{2}\big|_y^{1,2} \quad \tfrac{\pi}{2}\big|_y^{2,3} \quad \tfrac{\pi}{2}\big|_x^3 \quad \tfrac{\pi}{2}\big|_y^3 \quad \tfrac{\pi}{2}\big|_x^{1,2,3} \quad \tfrac{\pi}{2}\big|_y^{1,2,3} \tag{5.2}$$

where the short hand $\frac{\pi}{2}|_x^1$ means the unitary operation of $\frac{\pi}{2}$ rotation on the first spin around the x axis.

Once all of the product operators have been shown to be experimentally accessible, it is necessary to determine their weighting from the NMR signal. Neglecting noise, the NMR signal for Alanine has 12 sinusoidal components with distinct frequencies; one for each spin and its positive and negative coupling to the remaining two spins. More specifically, these frequencies ω_{ijk} are found from the internal Hamiltonian [17].

$$\omega_{ijk} = \frac{1}{2}\omega_{oi} \pm \pi J_{ij} \pm \pi J_{ik} \tag{5.3}$$

where i,j,k are different permutations of the vector [1 2 3]. The signal will also have phase information stored within its real and imaginary parts. Finally, the NMR signal has an

Rotation	Normal	Robust
$\frac{\pi}{2}\|_x^1$	0.975	0.992
$\frac{\pi}{2}\|_x^3$	0.983	0.998
$\frac{\pi}{2}\|_x^{1,2}$	0.968	.996
$\frac{\pi}{2}\|_x^{2,3}$	0.985	1.003
$\frac{\pi}{2}\|_x^{1,2,3}$	0.970	1.002
$\pi\|_x^{1,2}$	0.966	0.995
$\pi\|_x^{2,3}$	0.971	1.000

Table 5.1: Correlations of seven pulses; robust and uncompensated. All of the robust pulses show an improved fidelity over uncompensated pulses. All values have an error margin of ±0.01.

exponential relaxation with time constant T_2. The signal's general form is;

$$S(t) = e^{(-t/T_2)} \sum_i \sum_j \sum_k c_{ijk} \cos(\omega_{ijk} t) + d_{ijk} \sin(\omega_{ijk} t) \tag{5.4}$$

The signal's spectra can be obtained by taking its Fourier transform. The result is a sum of 12 Lorentzians each described by two parameters; the magnitude of its real and imaginary parts. These 24 parameters map linearly to the coefficients of the 24 observables. For example, the coefficient to σ_{x1} is the average of the magnitudes of the four Lorentzians with highest frequency.

5.3 Experimental Results

Two sets of seven pulses were made. The first did not compensate for RF inhomogeneity while the second did. Quantum Process Tomography was done on each of the fourteen pulses. To cut down on experiment time, only three of the 64 input states. These states are $\sum_i \sigma_{xi}$, $\sum_i \sigma_{yi}$, and $\sum_i \sigma_{zi}$. The resulting correlations were calculated and are presented in 5.3. All of the robust pulses yielded correlations greater than their uncompensated counterparts. The average improvement in the correlation is 0.024. This is well beyond the estimated error margin of ±0.01.

5.4 Degree of Improvement in RF Inhomogeneity Compensation

As stated in the previous section, the experimental fidelity was improved by using pulses robust towards RF inhomogeneity. Figure 5-3 summarizes the estimated error contributions of all the pulses. Of the five major error types, coherent errors, pulse distortions, measurement errors, decoherence, and RF inhomogeneity, the last was the greatest in magnitude. After compensation, it was reduced by approximately a factor of six. This is about the same as the magnitude of measurement errors. The combination of these two method reduced errors by approximately 60 percent.

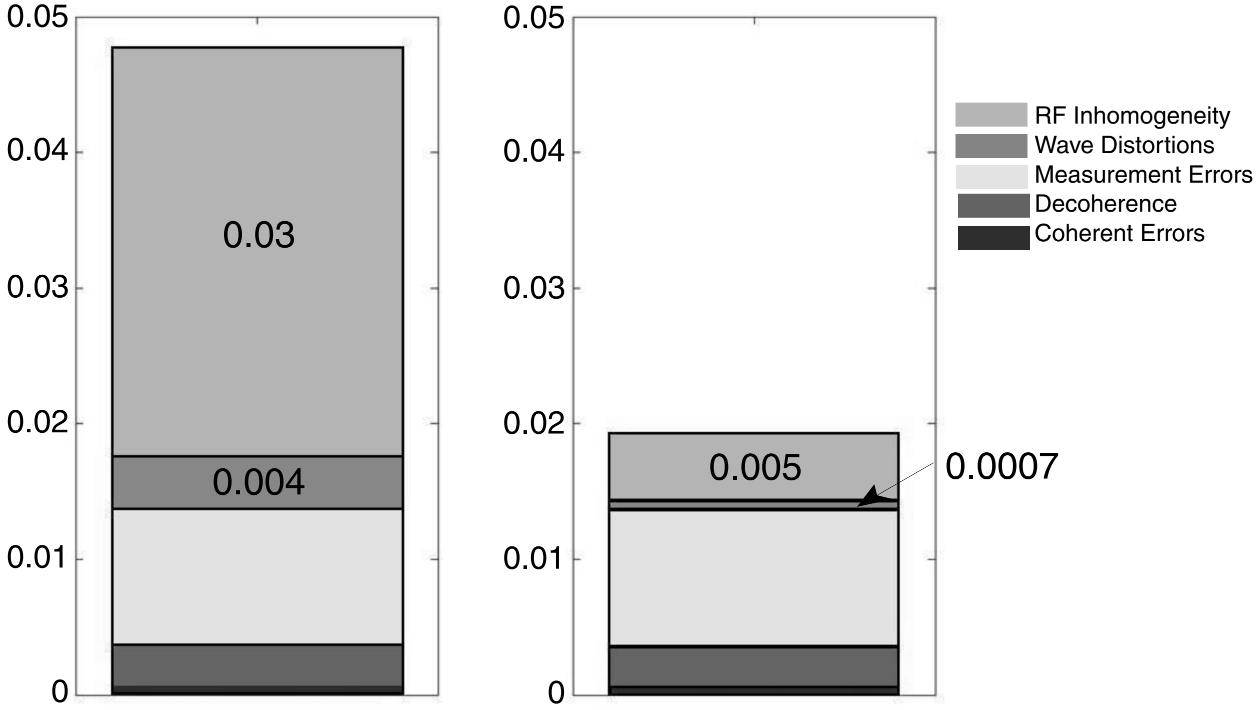

Figure 5-3: A Summary of Pulse Performance. On the left is pulses found without RF inhomogeneity compensation. On the right is pulses found with RF inhomogeneity compensation.

Chapter 6

Discussion

Chatpers 3 and 5 showed the theoretical and experimental performance of pulses that implement evolutions that are robust towards incoherent errors. Theoretically, they show well maintained fidelities in the presence of RF inhomogeneity, and experimentally high correlation values were measured. This chapter will continue by showing further aspects of these robust pulses, and it will try to propose extensions to other problems while illuminating the method's limitations.

6.1 Further Aspects of Pulse Performance

Chapter 3 showed previously in Figure 3-4 that the algorithm yields a set of robust pulse parameters. Specifically, performance is maintained as the RF inhomogeneity strength is varied. This, however, does not predict the performance of the pulse parameters when RF coil is perfectly homogeneous but has systematic bias in its power. Figure 6-1 shows the fidelity of the pulse as its power is amplified by a constant factor.

As expected the uncompensated pulses show a sensitivity to the scaling of the RF pulse power. Comparatively, the robust pulses maintain their fidelity especially for attenuations of the pulse power. Interestingly, the robust pulses on average perform best with a constant attenuation of about 3 percent. This is close to the average power of 3.50 percent attenuation delivered by the RF coil. Finally, this asymmetry of the robust pulses, in comparison to the symmetry of the compensated ones, suggests that it is due to asymmetry of the RF coil's power density function. In fact, this result correlates to the power density function's steep drop off near unity and its long tail that extends to a factor of 0.85. From this it is

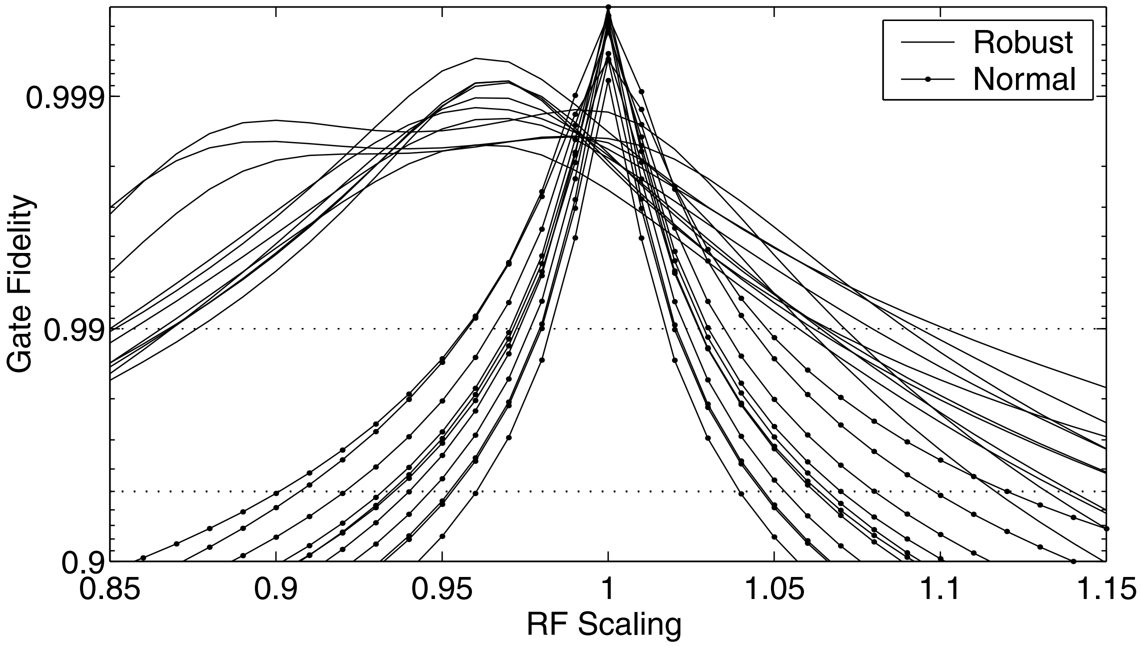

Figure 6-1: The fidelity performance of 11 robust and 11 uncompensated pulses as their RF power is scaled by a constant factor. The robust pulses show a greater ability to maintain fidelity especially at attenuated RF powers.

reasonable to conjecture that this algorithm would yield the opposite asymmetry if given a power density function with an excess of higher powers.

6.2 Pulse Fidelity in the Presence of Temporally Incoherent Errors

The above figure also suggests a robustness towards some time types of temporally incoherent errors. One can imagine an experimental situation where many pulses are cascaded and the pulse power varies but at a rate significantly slower than the duration of the pulse. In this instance, each pulse individually will create an evolution robust to the variation in the pulse power; and the train of pulses as a whole will more closely approximate the desired evolution than a train of pulses that did not compensate for incoherent errors. This argument is of great importance because QIP requires the use cascaded unitary operations that implement a series of one and two qubit quantum gates.

6.3 Exploring Achievable Fidelities

The proposed algorithm shows a good way of finding optimal RF pulse parameters in the presence of incoherent errors. Additionally, it can be repeatedly used to understand the depth and frequency of optimal points in the search space. Specifically, pulses can be found as the search constraints are relaxed and tightened; thereby simulating this method's achievable limits of control using a variety of equipment. A perfectly homogenous coil was assumed and the a set of parameter guesses was made using all of the previously mentioned intervals. While varying the second term in the power penalty function, these guesses were used to find pulses that implement a 90 degree rotation on Alanine's second carbon spin. Effectively, the upper limit on allowed powers was varied. Figure 6-2 shows the maximum fidelities of these pulses as a function of their maximum power. A total of 2088, 1222, and 599 pulses were made for 300, 600, and 800 MHz magnets respectively. While this method does not ensure finding globally optimal fidelities, the maximal fidelity among many local maxima provides an approximation of the maximum fidelity envelope in the absence of an

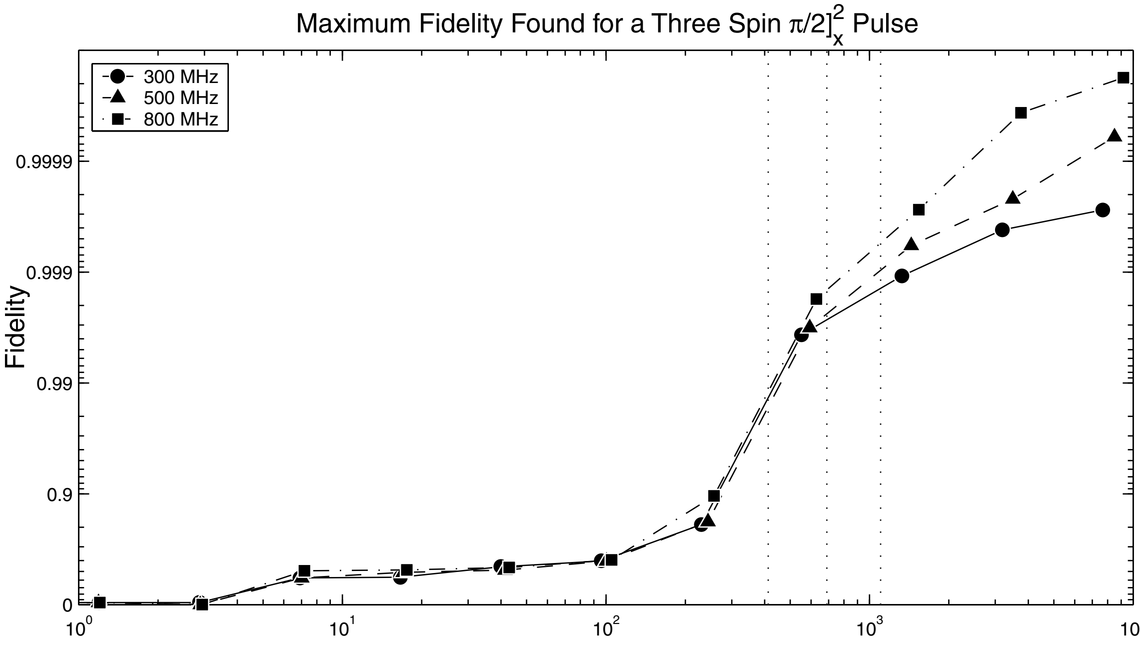

Figure 6-2: Maximum Fidelities found as function of Maximum Power.High fidelity pulses were found in high power regime defined by the minimum chemical shift difference.

analytical result. The dotted vertical lines show the minimum chemical shift difference for alanine on 300, 600 and 800 MHz magnets. The achievable fidelities drop dramatically in a low power regime defined by alanine's minimum chemical difference. For this molecule's high power regime, this algorithm is theoretically capable of achieving fidelities of at least 0.999. It appears that increasingly better fidelities can be achieved when a number of durations with increasingly loose power restrictions are used. Finally, significantly better fidelities were found for higher fields. As the static magnetic field strength is increased, the chemical shift differences increase with respect to the constant scalar coupling leading to a greater ability to make selective rotations. For an 800 MHz magnet, theoretical fidelities greater than 0.9999 were achieved. This is the degree of precision required for some estimates of fault tolerance.

6.4 Further Applications of Algorithm

This method does have general properties that give it applicability to other fields. First, NMR's external Hamiltonian together with the scalar coupling is able to control the system to any given state. These are two requirements for any experimental realization of quantum control. Secondly, the parameterization of amplitude, phase, frequency and time is non-specific to NMR. (Amplitude and phase of σ_x is equivalent to two amplitudes of σ_x and σ_y.) Together with the spin spin coupling, the amplitude and phase fully control operators that do not commute with the chemical shift Hamiltonian. Additionally, the frequency controls the chemical shift Hamiltonian itself. Other applications need only have 1.) parameters in the external Hamiltonian that together with qubit coupling control the non-commuting operators and 2.) a parameter that varies the extent of the commuting operator. This of course requires that the system Hamiltonian be well known in advance but not be the same as the liquid state NMR Hamiltonian.

This algorithm can also be applied in the field of classical feedback control. The state feedback equation of motion is [32] ,

$$\dot{x} = Ax + Bu \quad u = Gx \tag{6.1}$$

This is mathematically equivalent to Schrodinger's equation where A is the internal Hamiltonian, x is the wave function, and BG is the external Hamiltonian. In this type of state feedback, there exists more than one set of values that place the system eigenvalues in the desired locations in phase space. This algorithm would yield a set of optimal values for the feedback gains that resulted in the desired unitary evolution.

Chapter 7

Conclusions and Recommendations

7.1 Conclusions

This thesis has taken steps to address the errors that arise in the experimental implementation of quantum algorithms. Specifically, it proposed a method that compensates for incoherent errors when the system Hamiltonian is well known and the error source is measurable. This algorithm was then used to create a new set of pulses. In simulation, all of the new pulses had errors approximately one order of magnitude smaller than pulses that did not compensate for RF inhomogeneity. Experimentally, correlations were improved by 0.024 on average. In total, errors due to RF inhomogeneity were reduced by a factor of six.

7.2 Recommendations

This limitations of this method should be further investigated. Specifically, it is not yet clear how the degree of compensation varies for arbitrary RF inhomogeneity. The pulses developed could also be used in future liquid state NMR experiments that illustrate quantum algorithms. They could also be used in investigations of decoherence in QIP and studies of quantum chaos. Lastly, this algorithm could be used in quantum and classical control applications that have similar linear equations of motion.

Appendix A

List of Variables

α_n	Simplifying Constant
α_k	A weighting factor on the RF Power
A_k	A Krauss Operator
$\vec{B}$	Magnetic Field
B_o	Strength of the Static Magnetic Field
B_1	Strength of the Applied Radio Frequency Magnetic Field
b_k	A fraction of the liquid state volume
c_+	Coefficient of Ground State in Spin Wavefunction
c_-	Coefficient of Excited State in Spin Wavefunction
E	Energy
F	Fidelity
γ	Gyromagnetic Ratio
$\mathcal{H}$	Lab Frame Hamiltonian
$\mathcal{H}'$	Rotating Frame Hamiltonian
$\mathcal{H}_{cs}$	Chemical Shift/Zeeman Hamiltonian
$\mathcal{H}_J$	J/Spin-Spin Scalar Coupling
$\widetilde{\mathcal{H}}$	Rotating Frame Effective Hamiltonian
$\mathcal{H}_{int}$	Internal Hamiltonian
$\mathcal{H}_{ext}$	External Hamiltonian
$\hbar$	Planck's Constant divided by 2π
i	Index to count spins

I	Identity Operator
I_k	Identity Operator on k^{th} Spin
j	Index to count spins
J_{ij}	Scalar Coupling Coefficient Between Spins i and j
k	Index to Discrete RF Inhomogeneity Levels
K_b	Boltzmann's Constant
l	Index to number of durations in a Robust Pulse
μ	Magnetic Moment
N	Number of Spings
N_+	Number of Spins in Ground State
N_-	Number of Spins in First Excited State
ω_0	Larmor Frequency
ω_1	Power of External Hamiltonian
ω_{rf}	Natural Frequency of Radio Frequency Magnetic Field
P	Projection, State Fidelity
$\|\psi\rangle$	Spin State, Wavefunction, Ket
$\langle\psi\|$	Adjoint Spin State, Bra
ρ	Lab Frame Density Matrix
$\widetilde{\rho}$	Rotating Frame Density Matrix
ρ_{out}	Output Density Matrix
ρ_{th}	Theoretical Output Density Matrix
$\sigma_x, \sigma_y, \sigma_z$	Pauli Spin Operators
T	Temperature
t	Time
τ	Duration of an Applied Operator
U_k	Unitary Operator indexed by RF Inhomogeneity Power
U_{net}	Unitary Operation Due to Total Hamiltonian
U_r	Rotating Frame Unitary Operator
U_{th}	Arbitrary Theoretical Unitary Operator
$\langle x\rangle$	Expectation Value of Arbitrary Operator x
$[X]$	Ensemble Average of Aribrary Operator X
w_+	Fraction of Spins in the Ground State

w_-	Fraction of Spins in the Excited State

Appendix B

Robust Pulse Parameters

$Pulse$	$Time(\mu s)$	$Power(kHz)$	$Phase(deg)$	$Frequency(kHz)$
$\frac{pi}{2}\|_x^1$	40.04	10.98	−201.39	6.79
	46.41	9.07	−334.73	3.88
	56.76	10.80	−229.27	−6.21
	55.11	8.24	−82.04	−0.10
	72.61	2.90	−100.70	−4.41
	49.40	10.98	−143.39	−6.43
	78.73	8.15	80.89	0.00

(B.1)

$Pulse$	$Time(\mu s)$	$Power(kHz)$	$Phase(deg)$	$Frequency(kHz)$
$\frac{pi}{2}\|_x^2$	43.76	11.31	−24.71	−4.19
	63.44	5.20	−53.89	−6.62
	32.97	8.00	22.25	1.52
	39.27	11.30	−135.57	−7.15
	35.95	11.31	15.18	−6.91
	39.51	4.52	19.82	−2.43
	37.36	11.31	130.82	−5.22

(B.2)

$Pulse$	$Time(\mu s)$	$Power(kHz)$	$Phase(deg)$	$Frequency(kHz)$
$\frac{pi}{2}\|_x^3$	42.85	9.94	-291.92	-6.60
	73.87	10.11	-62.27	2.68
	45.29	6.97	-41.59	4.84
	53.60	7.19	-162.17	2.70
	84.45	10.12	-52.68	-6.84
	96.59	3.69	58.40	-2.19

(B.3)

$Pulse$	$Time(\mu s)$	$Power(kHz)$	$Phase(deg)$	$Frequency(kHz)$
$\frac{pi}{2}\|_x^{1,2}$	34.03	4.35	-76.66	0.04
	34.74	4.17	-41.12	-0.01
	44.66	5.28	-23.63	-10.05
	44.42	11.02	76.51	-9.78
	32.78	10.33	398.12	8.44
	33.69	10.47	269.01	8.51
	60.29	10.99	217.77	-0.74
	35.98	8.93	47.11	4.56

(B.4)

$Pulse$	$Time(\mu s)$	$Power(kHz)$	$Phase(deg)$	$Frequency(kHz)$
$\frac{pi}{2}\|_x^{2,3}$	49.17	11.25	299.63	4.51
	35.56	11.25	-332.05	-6.51
	35.58	10.82	-246.61	-5.97
	55.12	8.23	-183.10	8.17
	45.23	11.02	-198.80	-9.71
	35.55	6.32	-137.94	-9.57

(B.5)

$Pulse$	$Time(\mu s)$	$Power(kHz)$	$Phase(deg)$	$Frequency(kHz)$
$\frac{pi}{2}\|_x^{1,2,3}$	49.84	6.68	1.69	1.41
	50.02	10.69	112.85	-6.24
	100.55	5.64	32.79	-3.40
	100.27	6.52	82.19	-7.50
	50.14	4.35	143.60	6.28
	50.39	10.62	11.98	6.84

(B.6)

$Pulse$	$Time(\mu s)$	$Power(kHz)$	$Phase(deg)$	$Frequency(kHz)$
$pi\|_x^1$	41.65	10.74	16.94	0.00
	48.47	3.68	86.13	0.34
	39.05	11.24	108.46	-7.05
	35.17	7.52	337.69	1.54
	35.17	11.24	281.69	9.15
	52.62	11.24	241.04	-2.92
	38.20	11.24	40.64	-5.53

(B.7)

$Pulse$	$Time(\mu s)$	$Power(kHz)$	$Phase(deg)$	$Frequency(kHz)$
$p\|_x^2$	26.96	10.30	25.91	-0.89
	27.53	8.18	-7.21	-0.03
	26.71	3.71	-174.47	6.96
	26.71	3.25	-66.21	2.84
	27.34	4.12	-306.33	9.93
	28.58	3.90	438.70	4.90
	27.43	3.29	-146.78	-0.58
	27.48	7.53	-1238.63	-5.38
	26.71	4.75	-0.30	-0.00
	26.71	7.09	57.56	2.74
	26.79	5.23	-42.37	6.79
	26.74	3.72	-10.81	-0.02

(B.8)

$Pulse$	$Time(\mu s)$	$Power(kHz)$	$Phase(deg)$	$Frequency(kHz)$
$pi\|_x^3$	40.05	9.61	6312.14	2.14
	44.60	3.66	6083.83	11.51
	69.21	6.56	6014.45	8.04
	40.67	6.45	6122.85	8.47
	41.62	5.67	5134.62	0.36
	68.12	10.64	4884.80	-6.18

(B.9)

$Pulse$	$Time(\mu s)$	$Power(kHz)$	$Phase(deg)$	$Frequency(kHz)$
$pi\|_x^{1,2}$	110.60	9.34	-125.33	-7.63
	44.63	5.88	-31.00	-1.65
	61.62	4.00	-46.17	-3.36
	51.12	7.19	20.40	-0.89
	87.92	9.01	-215.76	-7.05
	71.37	5.58	-68.98	6.65
	57.27	8.91	22.83	3.51

(B.10)

$Pulse$	$Time(\mu s)$	$Power(kHz)$	$Phase(deg)$	$Frequency(kHz)$
$pi\|_x^{2,3}$	32.73	7.91	-451.34	1.35
	32.15	7.56	-453.94	1.07
	40.35	10.82	-302.37	-5.51
	32.16	8.87	-192.24	-11.90
	33.12	10.82	-201.02	1.84
	54.82	10.73	-200.28	-11.99
	33.56	7.94	221.17	2.67
	32.16	5.22	205.46	-10.56

(B.11)

Appendix C

Uncompensated Pulse Parameters

$Pulse$	$Time(\mu s)$	$Power(kHz)$	$Phase(deg)$	$Frequency(kHz)$
$\frac{pi}{2}\|_x^1$	37.92	8.71	138.61	-10.62
	44.57	10.77	233.21	-0.56
	63.70	10.77	62.76	0.05

(C.1)

$Pulse$	$Time(\mu s)$	$Power(kHz)$	$Phase(deg)$	$Frequency(kHz)$
$\frac{pi}{2}\|_x^2$	88.23	10.13	-174.94	-6.23
	79.82	4.29	-198.08	-6.06
	46.93	7.04	-88.44	-0.22
	42.32	3.61	37.69	0.48

(C.2)

$Pulse$	$Time(\mu s)$	$Power(kHz)$	$Phase(deg)$	$Frequency(kHz)$
$\frac{pi}{2}\|_x^3$	92.07	3.99	6078.35	-10.33
	76.97	5.70	6013.44	-1.86
	84.57	6.11	5235.81	-2.51

(C.3)

$Pulse$	$Time(\mu s)$	$Power(kHz)$	$Phase(deg)$	$Frequency(kHz)$
$\frac{pi}{2}\|_x^{1,2}$	47.87	5.07	18.72	-4.67
	57.09	6.66	130.05	1.60
	54.01	4.67	204.71	8.56
	67.51	5.63	-2.10	0.54

(C.4)

$Pulse$	$Time(\mu s)$	$Power(kHz)$	$Phase(deg)$	$Frequency(kHz)$
$\frac{pi}{2}\|_x^{2,3}$	38.84	5.69	144.62	−0.04
	52.84	10.59	−272.07	−2.33
	88.65	7.36	−67.69	0.06

(C.5)

$Pulse$	$Time(\mu s)$	$Power(kHz)$	$Phase(deg)$	$Frequency(kHz)$
$\frac{pi}{2}\|_x^{1,2,3}$	37.91	9.18	376.46	0.65
	84.38	9.34	55.40	−14.32
	39.48	8.13	19.82	−6.42
	103.46	7.28	223.82	2.36

(C.6)

$Pulse$	$Time(\mu s)$	$Power(kHz)$	$Phase(deg)$	$Frequency(kHz)$
$pi\|_x^1$	110.99	5.74	34.08	−5.14
	67.38	9.40	370.88	5.46
	56.06	9.96	−42.06	−9.87

(C.7)

$Pulse$	$Time(\mu s)$	$Power(kHz)$	$Phase(deg)$	$Frequency(kHz)$
$p\|_x^2$	43.41	6.82	112.14	−7.03
	121.45	7.35	143.48	7.41
	91.57	4.55	129.28	−1.66

(C.8)

$Pulse$	$Time(\mu s)$	$Power(kHz)$	$Phase(deg)$	$Frequency(kHz)$
$pi\|_x^3$	82.68	3.28	120.91	−0.45
	97.14	2.72	319.05	−1.04
	85.19	4.46	229.56	0.07

(C.9)

$Pulse$	$Time(\mu s)$	$Power(kHz)$	$Phase(deg)$	$Frequency(kHz)$
$pi\|_x^{1,2}$	29.34	10.55	0.00	0.29
	29.33	7.82	−152.43	−1.73
	30.31	4.15	18.34	−0.05
	29.37	9.63	143.23	1.07
	31.13	4.59	36.12	0.90
	32.38	3.25	69.80	0.06
	100.43	4.24	−27.15	0.00

(C.10)

$Pulse$	$Time(\mu s)$	$Power(kHz)$	$Phase(deg)$	$Frequency(kHz)$
$pi\|_x^{2,3}$	43.40	3.74	−137.12	6.91
	43.59	9.05	−129.59	0.05
	40.98	8.79	−169.63	−3.57
	40.98	10.06	−112.30	−8.74
	65.10	3.63	74.22	3.51

(C.11)

Bibliography

[1] R.P. Feynman. *International Journal of Theoretical Physics.* 21, 467, 1982.

[2] L. Grover. *Proceedings 28th Annual ACM Sumposium on the Theory of Computing STOC.* 212, 1996.

[3] P.W. Shor. *Siam. Journal of Computing.* 26, 1997, quant-ph/9508027.

[4] S. Lloyd. *Science.* 273. 23. August. 1996.

[5] A.F.Haught. *Annual Review of Physical Chemistry.* 19, 343, 1968.

[6] W.S. Warren, H. Rabitz, and M. Dahleh. *Science.* 259, 1581-1589, 1993.

[7] I.I. Rabi, S. Millman, P.Kusch, and J.R. Zacharias. *Physical Review* 55, 526, 1939.

[8] U. Haberlen, and J.S. Waugh. *Physical Review* 175, 453-67, 1968.

[9] E.M. Fortunato, M.A. Pravia, N.Boulant, G.Teklemariam, T.F. Havel and D.G. Cory. *Journal of Chemical Physics.* 116, 17, 7599-7606, 2002.

[10] W.S. Warren. *Science.* 242, 878-84, 1988.

[11] D.G. Cory, W. Maas, M. Price, E. Knill, R. Laflamme, W.H. Zurek, T.F.Havel and S.S.Somaroo. *Physical Review Letters*81, 2152-2155, 1998.

[12] E. Knill, R. Laflamme, R. Martinez and C.Negrevergne. *Physical Review Letters.* 86, 5811, 2001.

[13] S. Somaroo, C.HTseng, T.F. Havel, R.Laflamme, and D.G. Cory. *Physical Review Letters.* 82, 5381-84, 1999.

[14] J.A. Jones, and M.Mosca. *Journal of Chemical Physics.* 109, 1648-1653, 1998.

[15] I.L. Chuang, N. Gershenfeld, M. Kubinec, and D. Leung. *Physical Review Letters*. 80, 3408-3411, 1998.

[16] Y.S. Weinstein, M.A.Pravia, E.M. Fortunato, S.Lloyd, and D.G. Cory. *Physical Review Letters*. 86, 1889-1891, 2001.

[17] J. Cavagnagh, W.J. Fairbrother, A.G.Palmer III, N.J.Skelton. *Protein NMR Spectroscopy: Principles and Practice.* Academic Press. 1996.

[18] D.G.Cory.

`http://mrix4.mit.edu/Cory/Teaching/920_notes/chapter1/chap1.htm`

[19] Sakurai, J.J. *Modern Quantum Mechanics* Adison Wesley. 1994.

[20] Young, Hugh D., Freeman, Roger A. *University Physics* Adison Wesley. 1996.

[21] Slichter, C.P. *Principles of Magnetic Resonance* Springer 1978.

[22] S. Lloyd Phys. Rev. Lett. 75, 346-9 (1995).

[23] E Knill, R. LaFalmme, and W.H.Zurek, *Science* 279, 342-5 (1998).

[24] B. Schumacher. *Physical Review A*. 54, 4, 2614-2628. (1996).

[25] E.L. Hahn. *Physical Review*. 9080, 580-594, 1950.

[26] H.Y.Carr, and E.M.Purcell. *Physical Review*. 94,630-638, 1954.

[27] S.Meiboom, and D.Gill. *Review of Scientific Instruments*. 29, 688-691, 1958.

[28] A.J.Shaka, J. Keeler and R.Freeman. Evaluation of a New Broadband Decoupling Sequence: WALTZ-16. *Journal of Magnetic Resonance*. 53, 313-340, 1983.

[29] M.H.Levitt. Composite Pulses. *Advances in Magnetic Resonance*. 1396-1411.

[30] M.A. Pravia, A.M.Farid, N.Boulant, J.Emerson, E.M.Fortunato, T.F.Havel, D.G Cory, S.Lloyd *Robust Gates for Quantum Information Processing* To Be Published.

[31] M.A. Nielsen and I.L. Chuang. *Quantum Computation and Quantum Information.* Cambridge University Press 2000.

[32] B. Friedland. *Control System Design.* McGraw-Hill, New York. 1986.